Collisional Perturbation of States in Atomic Ytterbium

By Derek F. Kimball

Advisor: Professor Dmitry Budker

An undergraduate thesis submitted to the

Department of Physics

at the

UNIVERSITY of CALIFORNIA at BERKELEY

1998

Table of Contents

Abstract

Results of an investigation of collisional de-excitation (quenching) of the metastable 6s6p $^3P_0$ state in atomic ytterbium with respect to helium and neon buffer gases are reported. We find upper limits for the quenching cross sections to be $s_{Yb-He} < 13\times10^{-22}$ cm^2 and $s_{Yb-Ne} < 8\times10^{-22}$ cm^2. The small collisional de-excitation cross sections may enable an ytterbium parity nonconservation experiment to be performed using a vapor cell. We have also measured the pressure broadening and shift of the 649 nm 6s6p $^3P_0 \rightarrow$ 6s7s $^3S_1$ transition and the 556 nm 6s^2 $^1S_0 \rightarrow$ 6s6p $^3P_1$ transition by helium and neon and studied optogalvanic spectra of the 649 nm transition.

Acknowledgments

I would like to sincerely thank my advisor, Professor Dima Budker, whose patient and enthusiastic help made this project both possible and great fun. I would also like to thank my colleague throughout much of this work, Don Clyde, who had tremendous skill in all the areas where I had none. I also received invaluable assistance from my fellow Budker group members: Chris Bowers, Damon Brown, Brian DeBoo, Tuan Nguyen, Simon Rochester, Misha Solarz, Jason Stalnaker and Valeriy Yashchuk. Dave DeMille and Max Zolotorev provided a lot of wisdom and guidance throughout the project, and kept us on our toes! Important contributions to early stages of the project were made by M. Lintz, made possible by the France-Berkeley fund. Thank you very much, all of you!!!

Most of all I would like to thank my loving family for all their support over the years!!!

I would also like to acknowledge the support of the Berkeley Physics Undergraduate Research Scholar Program and the University of California at Berkeley Undergraduate Research Apprentice Program.

This work has been supported by UC Berkeley Committee on Research and the LBNL Nuclear Science Division under U.S. Department of Energy Contract No. DE-AC03-76SF00098.

I. CHAPTER ONE: Introduction

A. *Background*

It has long been the goal of physics to understand the fundamental constituents of matter and the nature of the interactions between them. Presently, physicists recognize four distinct interactions -- gravitation, electromagnetism, the strong force and the weak force -- and two general classes of particles which experience these interactions -- fermions and bosons. It was reasoned that these forces and particles respected certain symmetries -- that under particular transformations their properties were invariant.

Consider for example the reflection of a physical system in a mirror (or more properly inversion of spatial coordinates through the origin). This transformation corresponds to application of the parity operator Π to the system. Applying the parity operator twice must return the system to its original state -- thus Π has the eigenvalues ± 1. Indeed, assuming $|y\rangle$ is an eigenstate of parity:

$$\begin{aligned} &\Pi|y\rangle = l|y\rangle \\ &\Pi\big(l|y\rangle\big) = l\big(\Pi|y\rangle\big) = l^2|y\rangle = |y\rangle \end{aligned} \qquad (1.1)$$

$$\therefore \; l = \pm 1.$$

Parity is conserved in all processes that respect mirror symmetry. This means that a parity conserving Hamiltonian H commutes with the parity operator Π, enabling one to find simultaneous eigenfunctions of both H and Π. For this reason, atomic states (determined by the electromagnetic interaction) can be assigned a definite parity -- even (+1) or odd (-1).

Although the symmetry of physical systems with respect to mirror reflection appears intuitive, in 1956 Lee and Yang -- motivated by the experimental observation of two nearly identical particles which differed only in the parity of their decay products -- proposed that the weak interaction may not conserve parity [1]. Later that year, C.S. Wu and her colleagues carried out a definitive experimental test, discovering that indeed the weak interaction maximally violates parity conservation [2].

The cause of the parity non-conservation (PNC) observed by C.S. Wu et. al. was the weak charged-current interaction mediated by the $W^{\pm}$ vector bosons. Soon after this discovery, Ya. B. Zel'dovich considered the effects of a hypothetical weak neutral current interaction on atomic systems, and pointed out that it would lead to optical rotation of the plane of polarization of light passing through a sample of atoms [3]. Zel'dovich concluded that the effect was too small to be measured with experimental techniques available at that time. However in 1974 -- when the Standard Electroweak Model proposed by Glashow, Weinberg and Salam predicted a neutral vector boson, the Z_0 [4], and neutrino scattering experiments indicated the existence of a neutral weak current [5] -- M.-A. Bouchiat and C. Bouchiat reanalyzed the possibility of studying PNC in atoms [6]. They discovered that PNC effects are significantly enhanced in atoms with large atomic number Z, the enhancement scaling approximately as Z^3. Additionally, significant advances in laser technology greatly improved the ability to perform precise spectroscopic measurements in atoms. Considering these factors, the Bouchiats concluded that it was now feasible to search for PNC in heavy atoms.

Based on this new analysis, a number of groups began extensive experimental efforts to look for parity violating effects in atoms. The first observations of atomic PNC

were made using optical rotation in bismuth vapor by Barkov and Zolotorev in Novosibirsk [7]. Observation of PNC in bismuth provided crucial evidence that helped establish the existence of a neutral weak current, and most importantly was one of the first indications of the parity-violating nature of the neutral weak interaction. Measurements of the parity violating electron-nucleon interaction by deep inelastic scattering of polarized electrons on deuterons and protons at SLAC [8], and finally the direct observation of the Z_0 at CERN [9], ultimately confirmed this prediction of the Standard Model.

Over the past 20 years, atomic PNC effects have been measured with increasing precision [10]. The measurements are important not only as tests of the Standard Model but also as sensitive probes of new physics. The latest Boulder Stark-PNC interference experiment in cesium [11] has measured PNC effects to 0.35%. When combined with atomic theory calculations to 1% precision [12], this measurement is sensitive to several possible extensions of the Standard Model [13]. Recently, the Boulder group performed measurements of several parameters that reduce the uncertainty in determination of the weak nuclear charge Q_W [14]. They find a 2.5σ discrepancy between the measured value of Q_W and the value predicted by the Standard Model. Clearly, this is cause for further investigation of atomic PNC effects. Additionally, the Boulder experiment reported the first observation of the nuclear anapole moment -- a parity violating coupling to the electromagnetic field caused by weak interactions within the nucleus, manifesting itself as a small nuclear spin-dependent contribution to atomic PNC amplitudes. Precise measurement of the nuclear anapole moments of various atoms provides a new technique

for investigating the weak interaction in the hadron sector, which is notably more difficult to study than weak interactions involving leptons [15].

More precise measurements of atomic PNC appear possible, providing sensitive probes of physics beyond the Standard Model. An excellent candidate for the study of PNC in atoms is the $6s^2\ {}^1S_0 \rightarrow 6s5d\ {}^3D_1$ forbidden M1 transition in atomic ytterbium [16]. Efforts are underway in this laboratory to measure PNC effects in Yb using the Stark-PNC interference technique in an atomic beam [17, 18]. It also appears possible to perform an Yb PNC experiment in a vapor cell -- allowing higher atomic densities and a long (~ 2 ms) time integration of the PNC signal by accumulating atoms excited to the $5d6s\ {}^3D_1$ state in the metastable $6s6p\ {}^3P_0$ state. The population of the metastable state can be efficiently probed by measuring absorption of laser light tuned to the 649 nm $6s6p\ {}^3P_0 \rightarrow 6s7s\ {}^3S_1$ transition (Figure 1.1).

This study assesses the feasibility of conducting an ytterbium PNC experiment in a vapor cell. For such an experiment to be advantageous, it is necessary that the metastable $6s6p\ {}^3P_0$ state be long lived with respect to collisional quenching to allow time integration of the PNC amplitude. Additionally we require that the 649 nm $6s6p\ {}^3P_0 \rightarrow 6s7s\ {}^3S_1$ transition is not greatly pressure broadened so that the population of the metastable state can be efficiently probed. We measure these parameters for helium and neon buffer gases and assess the prospects for an ytterbium PNC cell experiment.

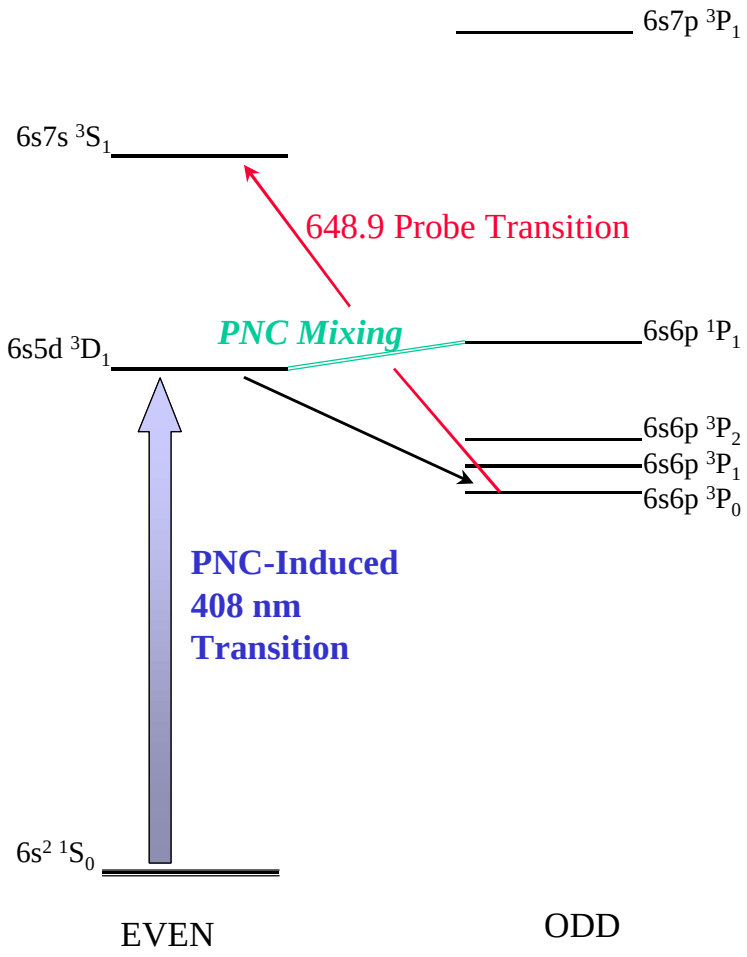

Figure 1.1 – *Partial energy level diagram for proposed ytterbium PNC experiment.*

B. *PNC in the 6s^2 $^1S_0$ ® 6s5d $^3D_1$ Transition in Atomic Ytterbium*

The 6s^2 ^{1}S$_0$ → 6s5d ^{3}D$_1$ transition in atomic ytterbium was proposed as a candidate for the study of atomic PNC effects by D. DeMille [16]. This is a promising system for the study of parity violation for a number of reasons. The 6s^2 ^{1}S$_0$ → 6s5d ^{3}D$_1$ transition is predicted to have a large PNC-induced $E1$ amplitude and suppressed $M1$ amplitude. The large $E1_{PNC}$ is due both to enhancement from high atomic number (Z=70)

and from an odd parity state of nominal configuration 6s6p $^1P_1$ lying near the upper 6s5d $^3D_1$ state of the transition ($\Delta E \sim 600$ cm^{-1}) [19]. The value of $E1_{PNC}$ for this transition is expected to be ~ 100 times larger than that in cesium. In principle, these advantages would allow measurement of PNC effects to an experimental accuracy of $\sim 10^{-4}$. Additionally, the seven stable isotopes of Yb enable us to measure PNC effects in a chain of isotopes -- thus allowing cancellation of atomic structure uncertainties by taking the ratio of PNC effects in different isotopes [20]. Hence the interpretation of PNC measurements with respect to new physics would be limited only by uncertainty in the nuclear neutron distribution.

1. Nuclear Spin Independent Effects

In the non-relativistic approximation and the limit of infinite Z_0 mass, the Hamiltonian H_{weak} describing the weak interaction between the nucleus and a single electron is given by [6]:

$$H_{weak} = \frac{G_F}{\sqrt{2}} \frac{1}{2m_e c} \frac{Q_W}{2} \vec{s}_e \cdot \left[\vec{p} d^3(\vec{r}) + d^3(\vec{r}) \vec{p} \right] + \textit{nuclear spin dependent terms}, \tag{1.2}$$

where G_F is the Fermi constant -- $G_F \cong 3 \times 10^{-12} m_e c^2 \left(\frac{\hbar}{m_e c} \right)^3$ -- m_e is the electron mass, $\frac{\vec{s}_e}{2}$ is the electron spin, $\vec{p}$ is the electron momentum, $\vec{r}$ is the electron position and Q_W is the nuclear weak charge.

In the Standard Electroweak Model, Q_W is given by:

$$Q_w(Z,N) \equiv -N + \left(1 - 4\sin^2 q_W\right) Z, \tag{1.3}$$

where q_W is the Weinberg mixing angle.

We note that due to the large mass of the Z_0, the atomic parity violating interaction manifests itself as a point-like potential ($H_{weak} \propto d^3(\vec{r})$). We can understand this aspect of atomic PNC by modeling the exchange of a Z_0 between the nucleus and an electron (Figure 1.2) as the creation and absorption of a Z_0 on a time scale short enough to not violate energy conservation. The Heisenberg Uncertainty principle states that:

$$\Delta E \Delta t \sim \hbar . \tag{1.4}$$

We let the uncertainty in energy be the minimum energy required to create a Z_0:

$$\Delta E \sim M_Z c^2 . \tag{1.5}$$

The length of time the Z_0 exists is given by Δt, so assuming the Z_0 travels near the speed of light, we find the range *r* of the neutral weak force:

$$\begin{aligned} \Delta t &\sim \frac{r}{c} \\ r &\sim \frac{\hbar c}{M_Z c^2} \sim \frac{197.3 \text{ MeV} \cdot \text{fm}}{91.2 \times 10^3 \text{ MeV}} \sim 2 \times 10^{-3} \text{ fm} \end{aligned} , \tag{1.6}$$

which on atomic (and even nuclear) scales is truly point-like.

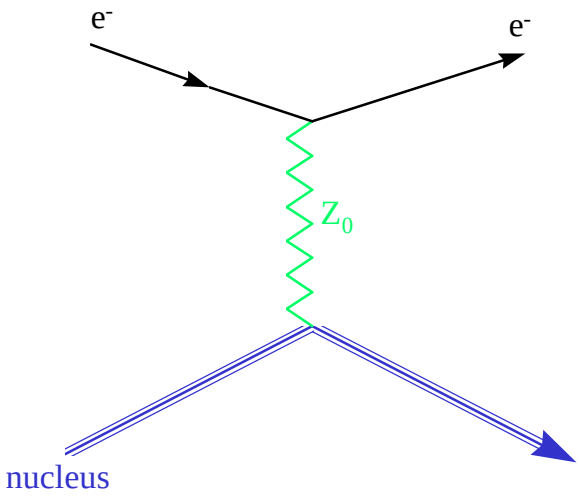

Figure 1.2 – *Electron interacting with the nucleus via the exchange of a Z_0.*

We can also directly see the parity violating nature of the weak interaction which arises from the $\vec{s}_e \cdot \vec{p}$ terms in equation (1.2). The electron spin $\frac{\vec{s}_e}{2}$ is an axial vector which does not reverse sign under the parity operator Π, whereas the electron momentum $\vec{p}$ is a polar vector which is taken to $-\vec{p}$ under Π (Figure 1.3). Therefore $\vec{s}_e \cdot \vec{p}$ is a pseudoscalar which reverses sign under spatial inversion. Hence:

$$H_{weak} \xrightarrow{Space\ Inversion} -H_{weak}\ ; \qquad (1.7)$$

H_{weak} does not commute with Π -- parity is not conserved.

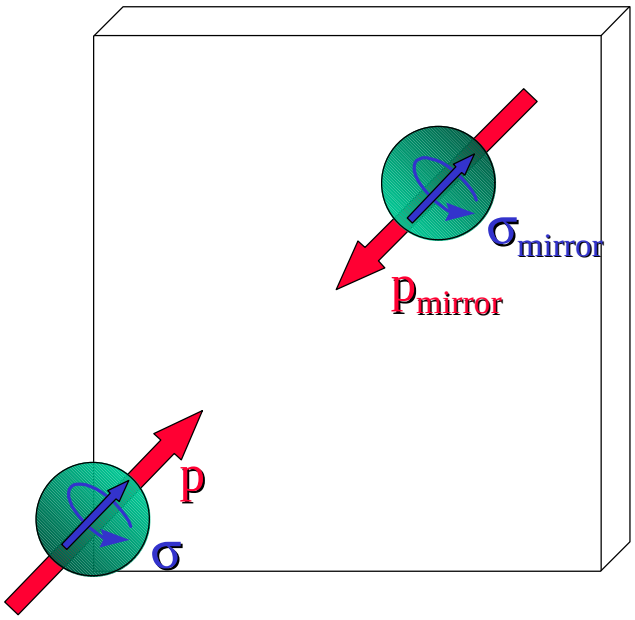

Figure 1.3 – *Electron reflected in a mirror. Under the parity operator P angular momentum remains the same since it is a pseudovector. Momentum, a polar vector, changes sign under P. Since the weak Hamiltonian is proportional to the inner product of these two quantities (equation (1.2)), it is manifestly P-odd.*

Due to the weak interaction, the electron wavefunctions derived from the parity-conserving electromagnetic interaction are no longer eigenstates of the Hamiltonian. As a small correction to the dominant electromagnetic force in an atom, the neutral weak electron-nucleus interaction can be treated as a perturbation that mixes states of opposite parity. Because of its point-like nature H_{weak} predominantly mixes $S_{1/2}$ states with $P_{1/2}$ states, since these states have the greatest probability amplitudes inside the nucleus.

In the independent particle model of the atom, states with $S_{1/2}$ electrons acquire an admixture of states with $P_{1/2}$ electrons, described by:

$$|ns_{1/2}\rangle \rightarrow |ns_{1/2}\rangle + \sum_{\text{p-states}} \frac{\langle n'\, p_{1/2}\,|H_{weak}|\,ns_{1/2}\rangle}{\Delta E}|n'\, p_{1/2}\rangle . \qquad (1.8)$$

From these arguments, we can understand the ~ Z^3 enhancement of PNC effects in heavy atoms. At the origin, the screening of the electromagnetic potential by outer electrons is negligible, so our electron wavefunctions differ from hydrogenic only in their normalization. Near the nucleus the electron velocity scales as:

$$v_e \sim Z \cdot a \cdot c . \qquad (1.9)$$

where a is the fine structure constant. Thus the electron momentum term $\vec{p}$ appearing in H_{weak} is proportional to *Z*, since the interaction occurs at the nucleus. The probability of an *s*-wave electron being within range of the nucleus to interact via the neutral weak current should be proportional to the electron density inside the nucleus ~ $|y_e(0)|^2$. In heavy atoms for the valence electrons $|y_e(0)|^2 \propto Z$, so the scaling of electron density near the nucleus contributes an additional factor of *Z*. Therefore, when we consider the mixing of states by the neutral weak force, we see that the matrix element indeed scales as Z^3. One Z term arises from the electron's momentum, a second from the electronic density inside the nucleus, and a third from the weak charge Q_W (equation (1.3)):

$$\langle n'\, p_{1/2}\,|H_{weak}|\,ns_{1/2}\rangle \propto |y_e(0)|^2 \cdot \vec{p} \cdot Q_W \propto Z^3 . \qquad (1.10)$$

Additionally, we see from equation (1.8) that PNC effects are enhanced when there is a small energy separation between opposite parity states. PNC effects in ytterbium are enhanced both by large atomic number (*Z*=70) and a small energy separation between opposite parity states.

In the case of ytterbium [16], we consider the forbidden $6s^2\ {}^1S_0 \rightarrow 6s5d\ {}^3D_1$ transition. The $6s5d\ {}^3D_1$ state is predominantly mixed with the nearby $6s6p\ {}^1P_1$ state (see Figure 1.1) which induces an $E1$ amplitude:

$$E1_{PNC} = \frac{\langle 6s5d\ {}^3D_1 | H_{weak} | 6s6p\ {}^1P_1 \rangle \langle 6s6p\ {}^1P_1 | z | 6s^2\ {}^1S_0 \rangle}{E({}^3D_1) - E({}^1P_1)} \tag{1.11}$$

At first glance, it appears there should be no PNC mixing between these states, since a *d*-wave electron is exchanged for a *p*-wave electron between the two states. However, it turns out that due to configuration mixing, there is a significant fraction of a 5d6p state admixed to the $6s6p\ {}^1P_1$ state. Thus PNC mixing occurs between the 5d6s component of the $^3D_1$ state and the 5d6p component of the $^1P_1$ state. The energy separation between the two states is $\approx 589\ \text{cm}^{-1}$, so $E1_{\text{PNC}}$ becomes:

$$E1_{PNC} = x \frac{\langle 6s_{1/2} | H_{weak} | 6p_{1/2} \rangle \langle 6s6p\ {}^1P_1 | z | 6s^2\ {}^1S_0 \rangle}{589\ \text{cm}^{-1}}, \tag{1.12}$$

where $x \approx 0.3$ is a parameter describing the configuration mixing amplitude and angular mixing coefficients. A semi-empirical estimate [16] finds:

$$\left| \text{Im}\left(E1_{PNC} \right) \right| \cong 1.1(4) \times 10^{-9}\ ea_0 . \tag{1.13}$$

Detailed theoretical calculations give the results:

$$\left| \text{Im}\left(E1_{PNC} \right) \right| \cong \begin{array}{ll} 1.09(25) \times 10^{-9}\ ea_0 & [21] \\ 0.75 \times 10^{-9}\ ea_0 & [22] \end{array}. \tag{1.14}$$

Compared to cesium, $E1_{\text{PNC}}$ in ytterbium is ≈ 100 times larger.

Uncertainty in the theoretical estimates of $E1_{\text{PNC}}$ for Yb is around 20%. Due to its closed *f*-subshell, the low-lying states of Yb are well described by a two valence electron model -- hence these predictions are reliable. However, there is little hope of improving

atomic theory calculations for Yb to a level better than a few percent in the near future. This severely limits the ability to interpret measurement of PNC effects in a single Yb isotope with regard to new physics. However, one can compare PNC effects between different isotopes [20] -- which removes any dependence on atomic structure. The ratio of $E1_{\mathrm{PNC}}$ between isotopes reduces to the ratio of the weak nuclear charges of the respective isotopes:

$$\frac{E1_{PNC}(N+\Delta N)}{E1_{PNC}(N)} = \frac{A_{atomic}\cdot Q_W(N+\Delta N)}{A_{atomic}\cdot Q_W(N)} = \frac{-N-\Delta N+Z\left(1-4\sin^2 q_W\right)}{-N+Z\left(1-4\sin^2 q_W\right)}. \quad (1.15)$$

At first it appears that such a measurement would constitute a direct determination of $\sin^2 q_W$. Further analysis [23] shows that in fact an uncertainty in the nuclear neutron distribution also plays a significant role. Since PNC effects arise from a contact potential and the electronic wavefunction has appreciable gradient over the nuclear size, PNC measurements quite sensitive to nuclear structure. Nuclear structure effects contribute an uncertainty of ≤1% to theoretical predictions. This creates limitations in an interpretation of an Yb PNC measurement comparable to those due to atomic theory uncertainty in the latest Boulder experiment in cesium [11, 14, 17]. However, there exist promising ways to reduce nuclear theory uncertainty by studying parity violating electron-nuclei scattering [17]. Another approach is to use PNC measurements themselves assuming the Standard Model to determine neutron distributions.

2. Nuclear Spin Dependent Effects

In addition to the nuclear spin independent effects discussed above, there arises a nuclear spin dependent contribution to $E1_{\mathrm{PNC}}$. This is primarily due to the anapole

moment of the nucleus [24], which arises from parity violating electromagnetic currents within the nucleus. The nuclear anapole moment can then interact with atomic electrons via the electromagnetic force (Figure 1.4). The magnetic field due to the anapole moment is zero outside the nucleus, so the PNC interaction due to the anapole manifests itself as a contact potential.

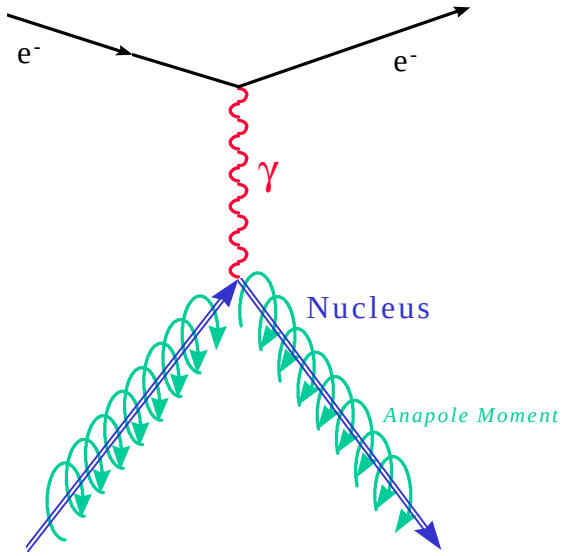

Figure 1.4 – *Parity violating nuclear anapole moment interacting with S-wave electron via the electromagnetic interaction.*

The P-odd potential arising from nucleon-nucleon weak interactions is, in the simplest shell model approximation for a valence nucleon, given by [21]:

$$H_{weak}^{nuclear} = \frac{G_F}{\sqrt{2}} \frac{g}{2m_p} \vec{s}_n \cdot \left[\vec{p} \cdot r(\vec{r}) + r(\vec{r}) \vec{p} \right], \tag{1.16}$$

where $r(\vec{r})$ is the density of core nucleons, $\frac{\vec{s}_n}{2}$ is the nucleon spin, $\vec{p}$ is the nucleon momentum, $\vec{r}$ is the nucleon position, m_p is the nucleon mass and $g \sim 1$ is a constant

which depends on the type of nucleon. The parity-violating nature of the interaction is evident from the appearance of the $\vec{s}_n \cdot \vec{p}$ terms. This interaction induces a current whose vector potential $\vec{\mathbf{A}}_a(\vec{r})$ is given by:

$$\vec{\mathbf{A}}_a(\vec{r}) = \vec{\mathbf{a}} d(\vec{r}) = \left(-p \int r^2 \vec{j}(\vec{r}) d^3 r\right) d(\vec{r}) . \tag{1.17}$$

$H_{weak}^{nuclear}$ (equation (1.16)) generates a nuclear anapole moment $\vec{\mathbf{a}}$ described by:

$$\vec{\mathbf{a}} = \frac{em}{2m_n} \frac{G_F}{\sqrt{2}} \frac{gA^{2/3}}{r_0} \frac{(I+1/2)(-1)^{(I+1/2-l)}}{I(I+1)} \vec{I} , \tag{1.18}$$

where $\vec{I}$ is the nuclear spin, m is the magnetic moment of the valence nucleon, l is the orbital angular momentum of the valence nucleon and r_0 is the nuclear radius (~10^{-13} cm). Since $\vec{\mathbf{a}}$ depends on the nuclear spin I, $E1_{\mathrm{PNC}}$ acquires a nuclear spin dependence [25].

Recently, Wieman and collaborators observed the effects of the anapole moment for the first time [11]. It showed up as a slight difference in $E1_{\mathrm{PNC}}$ between two hyperfine transitions in cesium:

$$\frac{\left|E1_{PNC}\right|}{b} = \begin{array}{l} 1.6349(80)\ \text{mV/cm}\ \ 6S(F=4) \rightarrow 7S(F=3) \\ 1.5576(77)\ \text{mV/cm}\ \ 6S(F=3) \rightarrow 7S(F=4), \end{array} \tag{1.19}$$

where b is the vector transition polarizability. A parameter κ indicating the relative size of the anapole moment, can be directly extracted from this measurement. The Cs data corresponds to $\kappa = 0.127 \pm 0.019$ [11], while calculations predict that $0.074 < \kappa < 0.095$ [26]. It is interesting to note that Cs anapole measurements do not appear to be consistent with measurements of the pion and isoscalar weak meson-nucleon couplings [15].

Clearly there is a need to measure nuclear spin dependent PNC effects to higher precision.

In ytterbium, a promising opportunity to study PNC effects due to the nuclear anapole moment exists. ^{171}Yb has I = 1/2 and for ^{173}Yb I = 5/2, so $E1_{PNC}$ can be compared between different hyperfine transitions in the odd isotopes. Also of interest is the fact that the valence nucleon in cesium is a proton, while in ytterbium it is a neutron, enabling one to study the parity violating nucleon-nucleon interaction in a different regime. The Yb PNC measurement would be sensitive to a different coupling constant than the Cs measurement. With $E1_{PNC}$ approximately 100 times larger in Yb than in Cs, it may be possible to measure nuclear spin dependent effects to a high accuracy, providing an important test of electroweak theory in the hadron sector.

C. *Yb PNC Experiment using a Vapor Cell*

Many of the Yb atoms (~ 70%) excited to the upper state of the $6s^2\ ^1S_0 \rightarrow 6s5d\ ^3D_1$ transition subsequently decay to the metastable $6s6p\ ^3P_0$ state (Fig. 1.1). One-photon radiative decays from the $6s6p\ ^3P_0$ state to the ground state are strictly forbidden by the J=0 $\nleftrightarrow$ J'=0 selection rule, so the lifetime of the metastable state is limited primarily by collisional quenching. Since most atoms excited to the $6s5d\ ^3D_1$ state accumulate in the metastable $6s6p\ ^3P_0$ state, it is possible to infer the $6s^2\ ^1S_0 \rightarrow 6s5d\ ^3D_1$ transition rate by monitoring the population of the $6s6p\ ^3P_0$ state. The population of the $6s6p\ ^3P_0$ state can be efficiently probed by measuring absorption of laser light tuned to the $6s6p\ ^3P_0 \rightarrow 6s7s\ ^3S_1$ transition (649 nm). This technique may enable an Yb PNC measurement to be performed in a vapor cell, offering a potential improvement in

statistical sensitivity to PNC effects compared to an experiment performed with an atomic beam.

In a vapor cell experiment, it is necessary to employ buffer gas to limit diffusion of Yb atoms from the probe region. Additionally, the buffer gas pressure must be high enough to allow application of sufficiently large electric fields without breakdown in order to observe the difference in $6s^2\ {}^1S_0 \rightarrow 6s5d\ {}^3D_1$ transition rates due to PNC-Stark interference. The optimal shot noise limited signal-to-noise ratio in measurement of the $6s6p\ {}^3P_0$ population by absorption of 649 nm light is achieved when there are two absorption lengths at 649 nm. This can be seen from the following argument. We want to measure the atomic density n (in our case the density of Yb atoms in the metastable $6s6p\ {}^3P_0$ state). For a given laser power P_0 and absorption cross section s, the light power P transmitted through the Yb vapor is described by:

$$P = P_0 e^{-l/l_0} = P_0 e^{-l \cdot ns}\ , \tag{1.20}$$

where l/l_0 is the number of absorption lengths, l being a parameter we can vary. The sensitivity to the probe light dP is proportional to the square root of the transmitted light power (counting error on the number of photons). From equation (1.20) for fixed l we find:

$$dP = P_0 \cdot (-ls \cdot dn) \cdot e^{-l/l_0}\ . \tag{1.21}$$

Setting $dP = \sqrt{P}$, with P from equation (1.20), we find for the sensitivity to density dn that:

$$dn \propto \frac{1}{\sqrt{P_0}} \frac{1}{ls} \cdot e^{l/2l_0}\ . \tag{1.22}$$

We want to minimize this quantity with respect to the number of absorption lengths:

$$\frac{\partial}{\partial l}\left(\frac{e^{l/2l_0}}{l}\right) \propto \frac{l}{2l_0} - 1 \equiv 0 \tag{1.23}$$

Therefore we find that maximum shot noise limited sensitivity to the number of atoms is achieved when $l = 2l_0$. This is because if we have too many or too few absorption lengths, the signal becomes insensitive to changes in the atomic density. If the 6s6p $^3P_0$ quenching rate and pressure broadening of the 649 nm probe transition are sufficiently small, it is possible to build up a large population of absorbing atoms at the probe frequency. This allows efficient detection of atoms having made the $6s^2\ ^1S_0 \rightarrow 6s5d\ ^3D_1$ transition.

In the present experiment, quenching cross sections of the 6s6p $^3P_0$ state and pressure broadening and shift of the 649 nm 6s6p $^3P_0 \rightarrow$ 6s7s $^3S_1$ transition with respect to helium and neon are measured, to our knowledge for the first time. The 6s6p $^3P_0$ state is populated by exciting Yb atoms from the ground state to the 6s7p $^3P_1$ state with a pump laser light pulse (Fig. 1.5), which subsequently populates the 6s6p $^3P_0$ state via cascade decay. The population of the 6s6p $^3P_0$ state is continuously monitored by measuring absorption of probe laser light at 649 nm. The quenching rate is determined from the time dependence of the 6s6p $^3P_0$ population. Measurements of the quenching rates at various buffer gas pressures and Yb densities yield limits on the Yb 6s6p $^3P_0$ quenching cross sections. The lineshape of the 649 nm transition in the vapor cell is found by measuring absorption with respect to probe beam frequency. Comparison of the 649 nm lineshape in the vapor cell to a reference line observed by optogalvanic spectroscopy in

an Yb hollow cathode lamp allows determination of the pressure broadening and shift of the 6s6p $^3P_0 \rightarrow$ 6s7s $^3S_1$ transition.

In addition, the pressure broadening and shift of the 556 nm 6s^2 $^1S_0 \rightarrow$ 6s6p $^3P_1$ transition is measured, also we believe for the first time (although there have been a number of studies of depolarizing and elastic cross sections of the 6s6p $^3P_1$ state [31-35]). In this case, comparison of absorption profiles in the vapor cell to fluorescence in an Yb atomic beam is used to calibrate frequency.

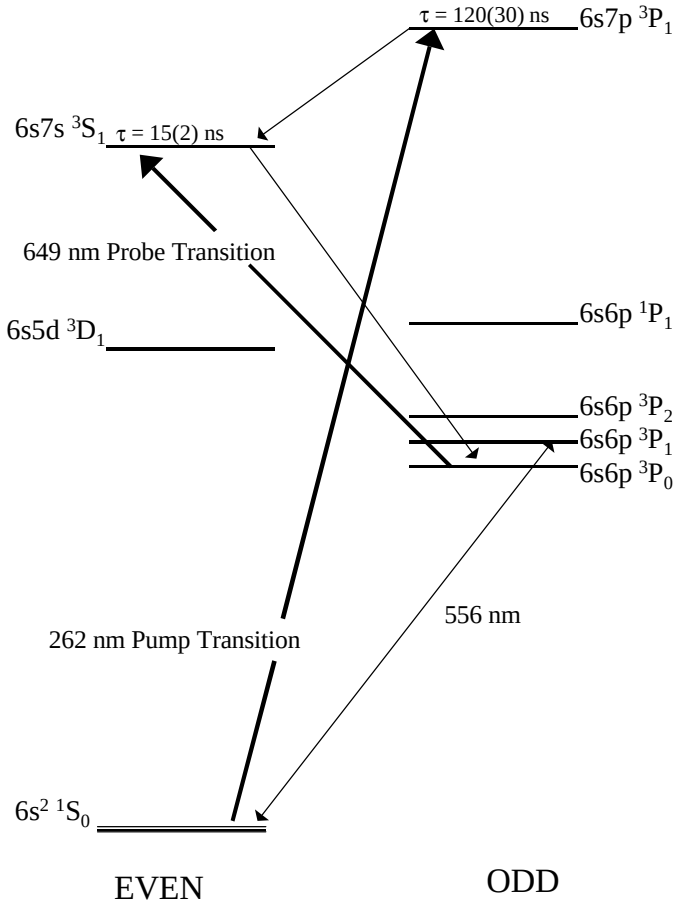

Figure 1.5 – *Partial energy level diagram of atomic ytterbium and relevant transitions for the measurement of collisional de-excitation cross sections of the 6s6p $^3P_0$ state. Lifetime of the 6s7s $^3S_1$ state is from [27-29], lifetime of the 6s7p $^3P_1$ state is from [30].*

CHAPTER TWO: Ytterbium Hollow Cathode Lamp

A. *Introduction*

The hollow cathode lamp (HCL) is a device that generates a gas discharge within a hollow cylindrical cathode. The inner surface of the hollow cathode is made from the material of interest (in our case ytterbium). When high energy ions ($\gtrsim$ 30 eV) in the discharge collide with the surface of the cathode, the cathode can eject ytterbium atoms (sputtering). Steady state ytterbium densities in the discharge are approximately 10^{11} atoms/cm^3 under normal operating conditions [1]. Collisions with energetic ions, electrons, and neutral atoms within the discharge populate many excited states within the discharge – making the hollow cathode lamp useful for a wide range of spectroscopic investigations.

A particularly useful application of the hollow cathode lamp is optogalvanic spectroscopy, where the discharge is irradiated by light resonant with an atomic or molecular transition of a species within the discharge. This produces a change in the conductivity of the discharge, creating an observable electronic signal – enabling a convenient technique for laser spectroscopy. Another application is as a light source, giving Doppler limited emission spectra (for Yb and Ne in our case).

In our experiments, the optogalvanic signal in an Yb HCL is used as a reference for tuning lasers to the $6s6p\ ^3P_0 \rightarrow 6s7s\ ^3S_1$ transition (649 nm) in ytterbium. The Yb HCL also provides known emission and absorption spectra useful for frequency calibration of lasers and spectrometers.

B. *Hollow Cathode Lamp Characteristics*

A schematic diagram of the commercial ytterbium hollow cathode lamp used in our experiments [2] is shown in Fig. 2.1. The hollow cathode lamp consists of an airtight glass envelope filled with neon (other types of lamps use other noble filler gases) at a pressure of about 20 Torr. In our case, the cathode has an ytterbium core and is surrounded by an absorbent shield that reduces ytterbium density outside the cathode (thereby reducing self-absorption by Yb atoms outside the discharge). A circular anode is suspended slightly above the hollow cathode by insulated supports.

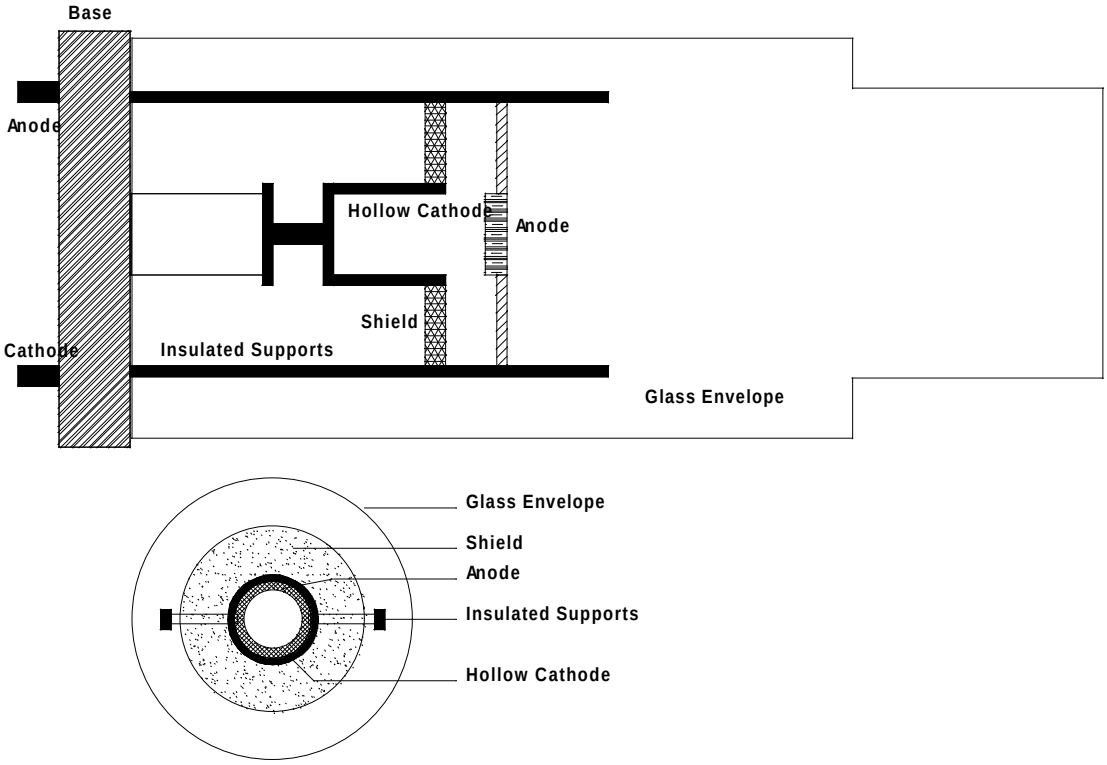

Figure 2.1 – *Schematic diagram of the hollow cathode lamp.*

The lamp is connected to a power supply (typically operating at 300 volts, corresponding to a steady state current of ~ 16-18 mA and a voltage drop across the HCL of ~ 170 volts) as shown in the circuit in Fig. 2.2. The setup allows monitoring of the current and voltage characteristics of the lamp with standard equipment and enables detection of the optogalvanic effect for laser spectroscopy.

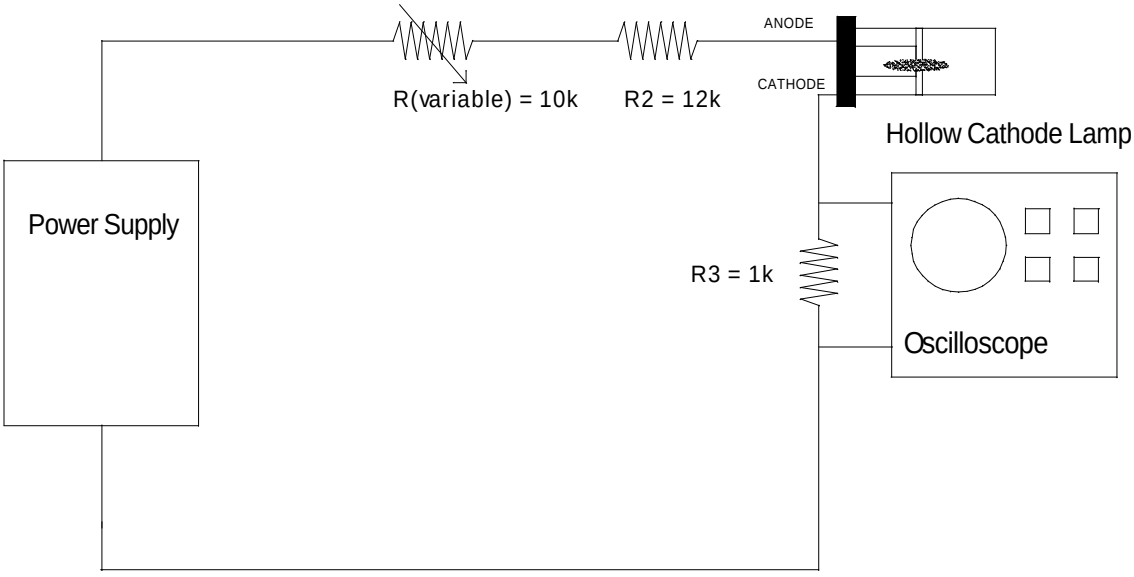

Figure 2.2 – *Hollow cathode lamp circuit for optogalvanic spectroscopy.*

A. Features of the Optogalvanic Effect

When light is absorbed by atoms in the hollow cathode discharge, the steady state population of atomic energy levels changes. The perturbation in energy level population alters the conductivity of the discharge (optogalvanic effect). There are two known mechanisms responsible for the optogalvanic effect [3]. In one mechanism, a change in the steady state energy level population changes ionization rates, which in turn alters the electron density. In the second mechanism, excitation of atoms to higher electronic states

perturbs the equilibrium established between electron temperature and atomic excitation temperature, thereby altering the average kinetic energy of electrons in the discharge. Energy is transferred from excited atoms to electrons via superelastic collisions. In superelastic collisions, electrons collide with atoms in excited states causing the atoms to undergo radiationless decays that transfer internal energy of the atom to the electrons, thereby increasing the electrons' kinetic energy. The relative importance of these two mechanisms depends on discharge and excitation conditions.

Both mechanisms directly depend on the photon absorption rate. Consequently, the amplitude of the optogalvanic effect is generally linearly related to the photon absorption rate under typical discharge conditions [4]. The optogalvanic amplitude is linear with respect to steady state current since both mechanisms depend linearly on the electron-atom collision rate, which is proportional to the electron density.

D. *Optogalvanic Spectroscopy with the Yb Hollow Cathode Lamp*

We have conducted several experiments investigating properties of the ytterbium hollow cathode lamp and the optogalvanic effect. A block diagram of the experimental setup is shown in Fig. 2.3. An Argon-ion pumped dye laser (Coherent Radiation CR599) was tuned to the 649 nm transition and the optogalvanic effect was observed with a digital oscilloscope. A laser beam chopper provided modulation of the optogalvanic signal allowing observation of relatively small changes in the current through the hollow cathode lamp. A digital lock-in detector [5] was used to record the optogalvanic signal amplitude at a given laser frequency. Fig. 2.4 shows the observed optogalvanic signal when the laser is tuned to resonance with the 649 nm $6s6p\ ^3P_0 \rightarrow 6s7s\ ^3S_1$ transition.

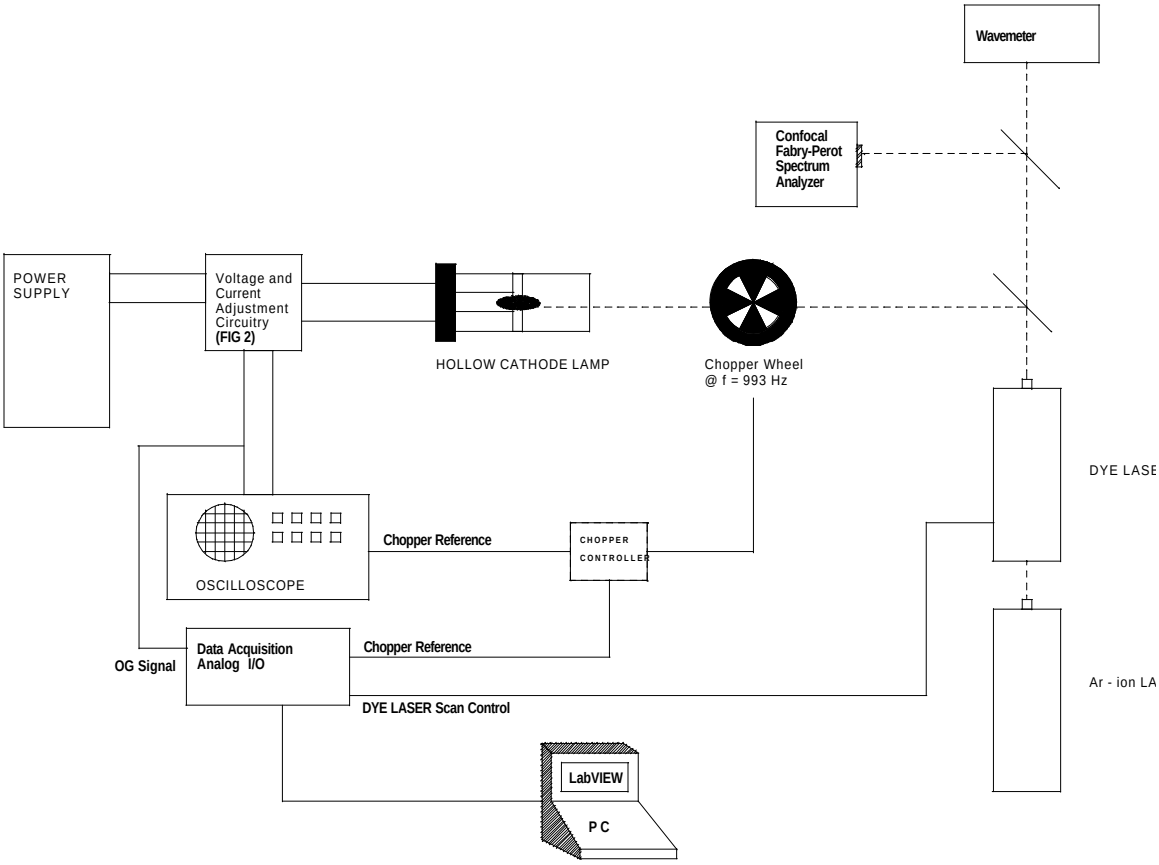

Figure 2.3 – *Block diagram of experimental set-up for optogalvanic spectroscopy of the Yb 649 nm 6s6p $^3P_0$ ® 6s7s $^3S_1$ transition.*

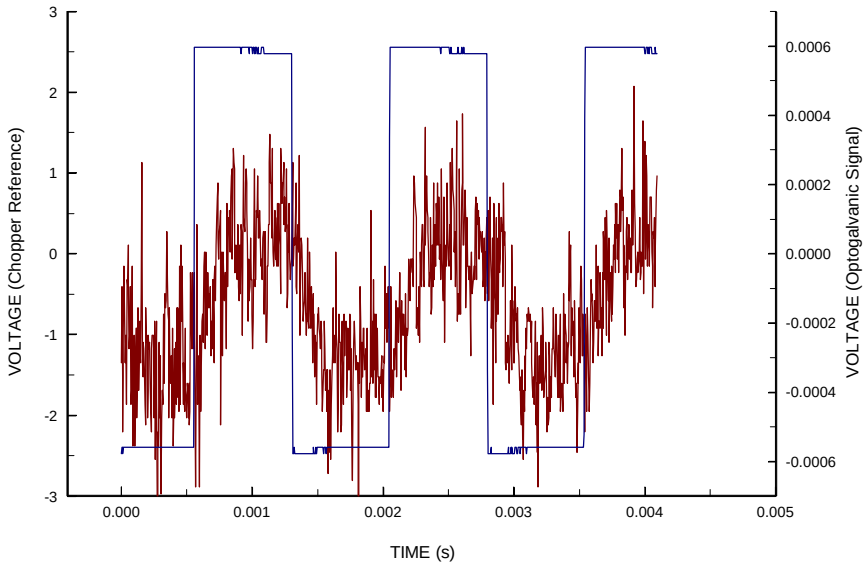

Figure 2.4 – *Optogalvanic signal: current = 15 mA, laser power = 3 mW.*

1. HCL Voltage and Optogalvanic Signal vs. Current

Adjusting the applied voltage from the power supply varies the current through the hollow cathode lamp. The voltage drop across the discharge remains relatively constant throughout the range of currents investigated (Fig. 2.5). This is due to the stability of the discharge processes in this regime. Increases in applied voltage are counteracted by increased ion-electron pair production, thereby decreasing the resistivity of the discharge. This enables the discharge to maintain a constant operating voltage.

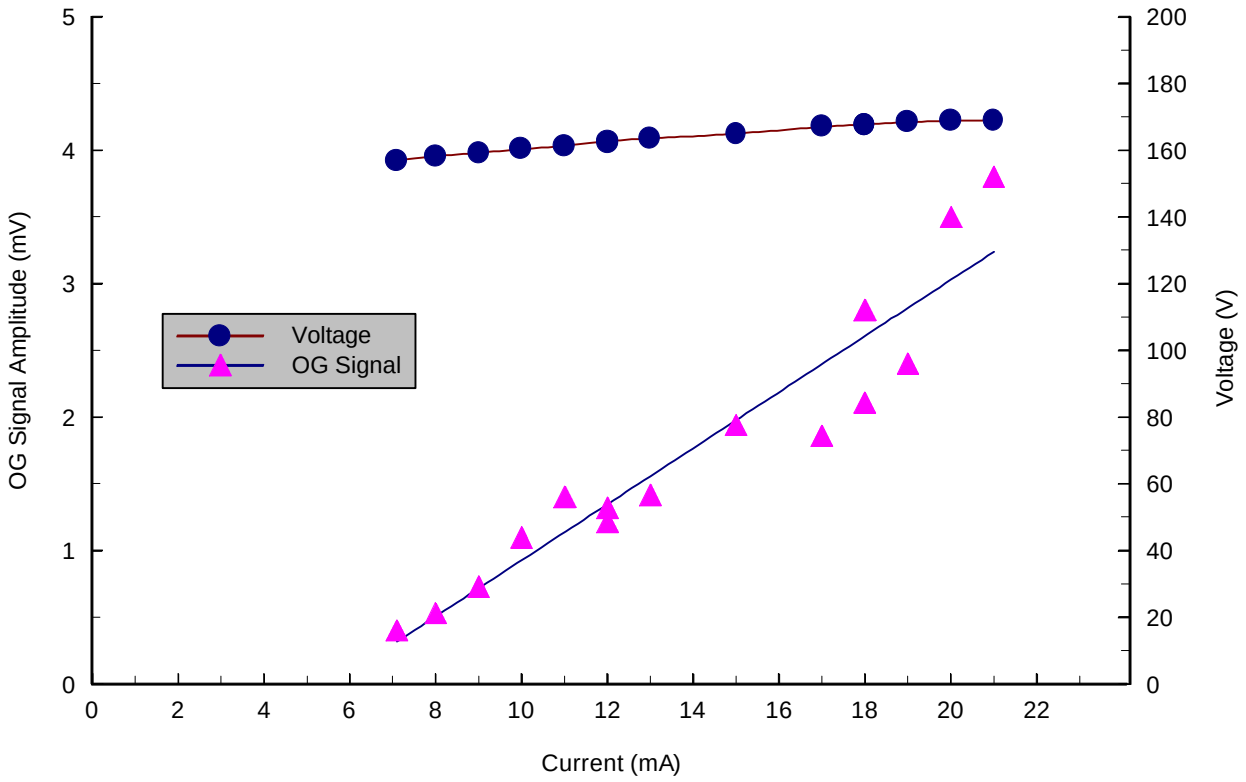

Figure 2.5 – *Voltage drop across the Yb HCL and optogalvanic (OG) signal amplitude with respect to current, laser power = 10 mW tuned to the center of the even isotope resonance (see Fig. 2.7).*

The optogalvanic signal amplitude was found to vary linearly with current. At a laser power of 10 mW tuned to the center of the even isotope component of the 649 nm transition, the ratio of optogalvanic signal current amplitude (ΔJ) to net current (J) through the HCL was measured to be:

$$\frac{\Delta J}{J} = 1.2(3)\times 10^{-4}.$$

2. Optogalvanic Signal vs. Laser Power

We also find a direct proportionality between incident laser light power and optogalvanic signal amplitude (Fig. 2.6). This relationship is consistent with theoretical models [3,4], so long as the 6s6p $^3P_0 \rightarrow$ 6s7s $^3S_1$ transition is not effectively saturated.

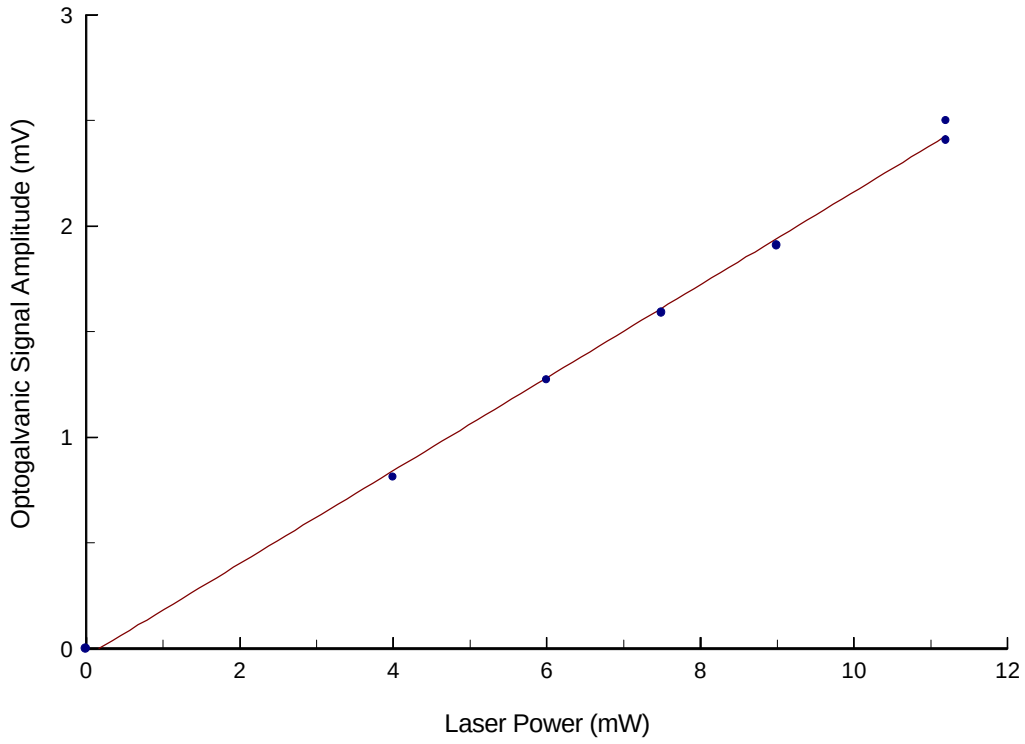

Figure 2.6 – *Optogalvanic signal with respect to laser power, current = 15 mA.*

This observation is consistent with the prediction of the saturation parameter. If we assume velocity-changing collisions play an important role, the saturation parameter S is given by:

$$S = \frac{\Omega^2}{g_D \Gamma_r}, \tag{2.1}$$

where $\Omega = \mathbf{D}_{if} \cdot \mathbf{E}_0 / \hbar$ is the Rabi flopping frequency, $\mathbf{D}_{if}$ is the induced dipole moment for the transition ($\mathbf{D}_{if} \sim ea_0$ for the 6s6p $^3P_0 \rightarrow$ 6s7s $^3S_1$ transition), $\mathbf{E}_0$ is the laser light electric field, γ_D is the Doppler width and Γ_r is the relevant relaxation rate. $\frac{\Omega^2}{g_D}$ is the optical pumping rate. The Doppler width obtained from fits to resonance lines in the HCL is $2\pi \times$ 400 MHz. At the highest measured laser power of ~ 12 mW (beam diameter ~ 0.2 cm) the pumping rate is ~ 3×10^7 s^{-1}. A lower limit on the dominant relaxation rate can be estimated by considering quenching of the 6s7s $^3S_1$ state by superelastic collisions with electrons.

Under typical conditions in a standard commercial HCL the electron density n_e in the discharge is ~ 10^{13} cm^{-3} [1]. Cross sections for superelastic electron scattering from excited states can be quite large (σ_{se} ~ 10^{-13} cm^2) [6]. Therefore we estimate the superelastic collisional de-excitation rate g_{se} to be:

$$g_{se} = v_e n_e s_{se} \approx 2 \times 10^8 \text{ s}^{-1}, \tag{2.2}$$

where $v_e \sim 2 \times 10^8$ cm/s is the mean electron velocity. Thus the saturation parameter S, given by equation (2.1), is less than 0.15, consistent with our observations. If velocity changing collisions are negligible, then S is given by:

$$S = \frac{\Omega^2}{\Gamma_r^2}.$$

In this case, *S* is also << 1, so in either case we do not expect saturation of the transition.

3. Hyperfine Structure and Isotope Shifts of the 6s6p $^3P_0 \rightarrow$ 6s7s $^3S_1$ transition

An 18-GHz laser scan across the 649 nm 6s6p $^3P_0 \rightarrow$ 6s7s $^3S_1$ transition yielded the optogalvanic spectrum shown in Fig. 2.7. The spectrum is assembled by concatenating the results of three overlapping 7.3 GHz scans. The isotope shifts and

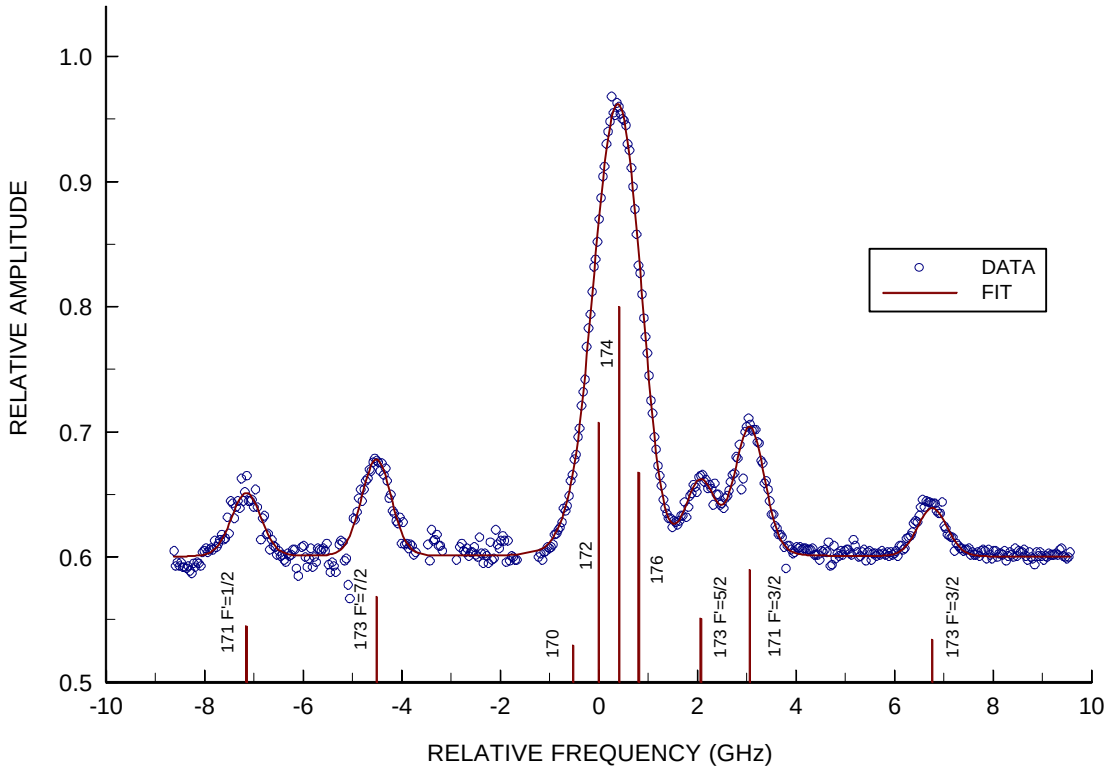

Figure 2.7 – *Optogalvanic spectrum of the Yb 649 nm 6s6p $^3P_0$ ® 6s7s $^3S_1$ transition. Isotopic components are labeled with the respective atomic masses and F' is the total angular momentum of the upper state of a hyperfine transition.*

hyperfine structure have been previously measured in [7-9], our results are in agreement with these earlier findings.

Each 7.3 GHz scan consists of 200 data points, each point the result of an optogalvanic signal amplitude averaged over 40 ms. The data is fit to a Voigt profile (discussed in Chapter 3). The frequency scaling was determined by fitting the lowest frequency peak and the highest frequency peak to the predicted ^{171}Yb F'=1/2 and ^{173}Yb F'=3/2 peaks respectively.

The calculated values of the hyperfine splitting, isotope shifts and total shifts are presented in Table 1. It should be noted that the values for the ^{173}Yb 7 $^{3}S_1$ hyperfine energy level splitting disagree with the values published in a similar table in [7]. It appears that this is merely due to a sign error in [7]. These values are consistent with our measurements.

TABLE 1: Hyperfine Structure and Isotope Shifts (calculated)

ISOTOPE	ISO. SHIFT	HF SHIFT	TOTAL SHIFT	REL. INTENSITY (calculated)
170	-0.524	None	-0.524	0.049
171	-0.345	(F' = 3/2) 3.405	3.06	0.15
		(F' = 1/2) –6.810	-7.155	0.075
172	0	None	0	0.346
173	0.185	(F' = 7/2) –4.698	-4.513	0.114
		(F' = 5/2) 1.881	2.066	0.085
		(F' = 3/2) 6.581	6.766	0.057
174	0.413	None	0.413	0.5
176	0.805	None	0.805	0.279

E. *Ytterbium Emission Spectrum Analyzed with a Grating Spectrometer*

Emitted light from the Yb HCL was coupled into a grating spectrometer (a Jarrel-Ash Czerny-Turner Model II) with a multi-mode optical fiber. A frequency range from 3900 nm to 6700 nm was scanned, and we observed the Yb transitions listed in Table 2, identified by comparison with [10]. Lines attributed to Ne are listed in Table 3. The primary purpose of these scans was to calibrate the spectrometer and determine observable transitions in the hollow cathode discharge.

TABLE 2: Observed Yb Emission Lines and Corresponding Transitions

WAVELENGTH(air)	TRANSITION			INTENSITY
3987.98 nm	$4f^{14}\ 6s^2\ {}^1S_0$	→	$4f^{14}6s^1 6p^1\ {}^1P_1$	weak .
4089.68	17992_1 (odd)	→	42436_0	weak
4149.07	19710_2 (odd)	→	43805_1	weak .
4174.56	17992_1 (odd)	→	41939_0	weak
4180.81	?	→	?	weak .
4231.97	17992_1 (odd)	→	41615_1	weak
4966.9	19710_2 (odd)	→	39838_2	*medium* .
5067.8	28184_4 (odd)	→	47911_5	weak
5074.34	24751_2	→	44453_3 (odd)	*medium* .
5184.15	?	→	?	weak
5505.49	24489_1	→	42647_2 (odd)	weak .
5539.05	?	→	?	weak
5556.47	$4f^{14}6s^2\ {}^1S_0$	→	$4f^{14}6s^1 6p^1\ {}^3P_1$	**strong** .
5568.11	25859_5 (odd)	→	43814_5	weak
5686.53	?	→	?	*medium* .
5719.99	27677_2	→	45155_2 (odd)	*medium*
5819.41	?	→	?	weak .
6643.55	27677_2	→	42725_2 (odd)	weak

TABLE 3: Observed Ne Emission Lines

WAVELENGTH(nm)	INTENSITY
5005.159	weak
5656.659	*medium*
5764.419	*medium*
5804.45	weak
5852.488	**strong**
5881.895	**strong**
5902.462	weak
5944.834	**strong**
5974.627	*medium*
5987.907	*medium*
6029.997	*medium*
6074.338	*medium*
6096.163	*medium*
6163.594	*medium*
6217.281	*medium*
6266.495	*medium*
6334.428	*medium*
6382.992	*medium*
6402.246	*medium*
6506.528	*medium*
6532.882	weak
6598.953	weak
6652.093	weak
6678.276	weak
6717.043	weak

An experiment to precisely measure the 5d6s $^3D_1 \rightarrow$ 6s6p $^3P_{2,1,0}$ branching ratios (to a few %) is currently in progess in this laboratory, using an Yb HCL filled with argon. Relative intensity of emission lines will be measured. Argon lines are used for spectrometer response calibration [11].

CHAPTER THREE: 6s6p $^3P_0$ Collisional Quenching Cross Sections and Pressure Broadening and Shift of the 6s6p $^3P_0 \rightarrow$ 6s7s $^3S_1$ Transition

A. *Experimental Setup*

The experimental apparatus for measuring the Yb collisional quenching cross sections and 649 nm 6s6p $^3P_0 \rightarrow$ 6s7s $^3S_1$ pressure broadening and shift is shown in Fig. 3.1. A few grams of Yb (natural abundance) are placed in the center of a resistively heated, tantalum-lined stainless steel vapor cell (Fig. 3.2). The ends of the cell are water

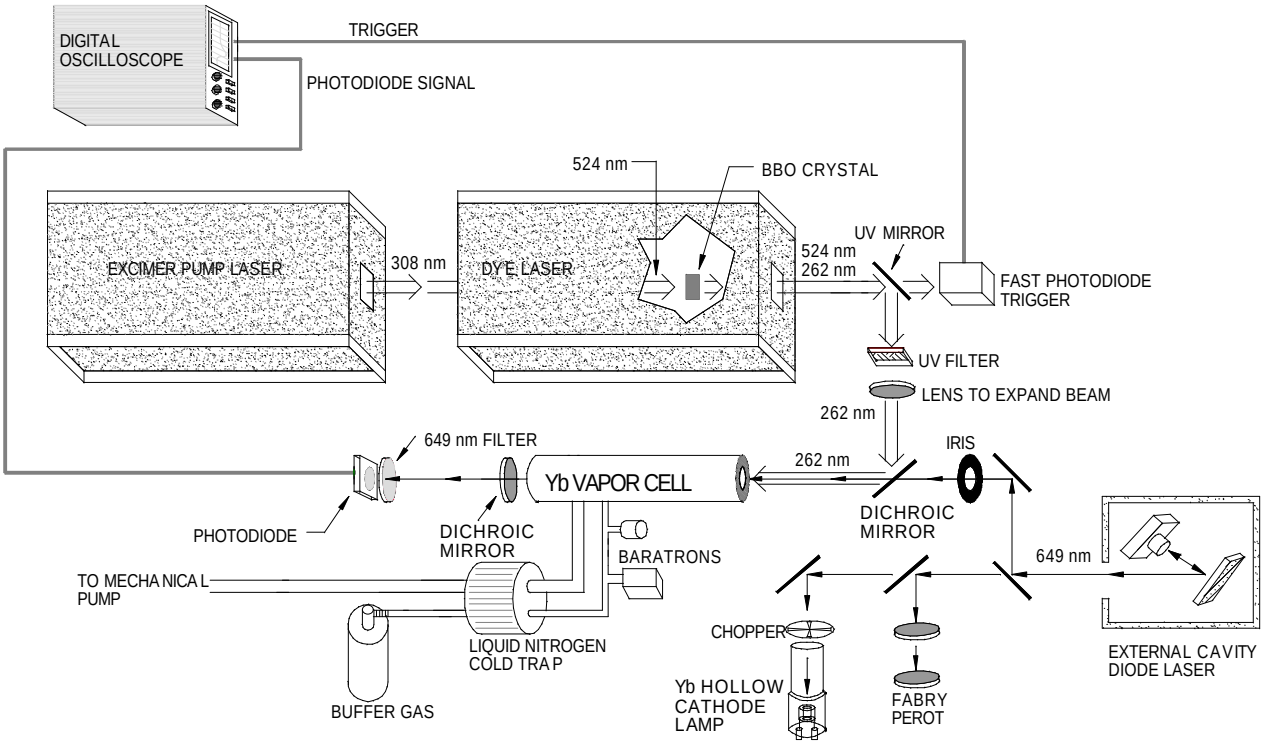

Figure 3.1 – *Experimental set-up for Yb 6s6p $^3P_0$ collisional de-excitation cross section and 649 nm 6s6p $^3P_0$ ® 6s7s $^3S_1$ pressure broadening and shift measurements.*

cooled. Fused silica windows are sealed at the ends of the cell with rubber o-rings. The vapor cell is pumped down to ~ 10^{-2} Torr with a mechanical vacuum pump and baked overnight at ~ 500 K in order to remove impurities. Before measurements are performed,

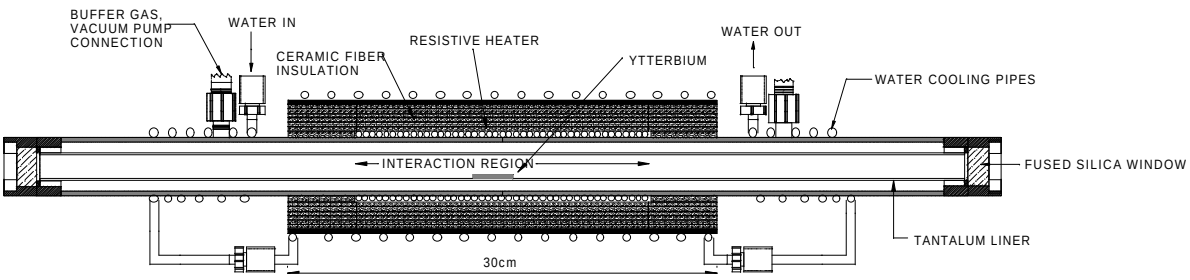

Figure 3.2 – *Scale drawing of the Yb vapor cell.*

the cell is repeatedly flushed with the buffer gas of interest. In order to reduce the introduction of impurities into the cell, all gas lines in and out of the vapor cell pass through a liquid nitrogen trap. A trap filled with steel wool is in line between the mechanical pump and the vapor cell to reduce cell contamination with vacuum pump oil.

When the ytterbium sample is exposed to atmosphere (prior to being placed in the vapor cell) it appears that a layer of refractory material forms on the outside of the sample. Because of this refractory layer, it is necessary to heat the cell to ~ 1000 K before we observe an ytterbium vapor pressure near the expected value. The vapor cell is subsequently cooled to 700 K in order to operate at the desired ytterbium density for quenching cross section and pressure broadening and shift measurements. Ytterbium in the central heated region sublimates and forms a vapor column. Outside the central region, water cooling reduces the cell temperature and ytterbium condenses into solid form (since the cell temperature is below the Yb melting point).

Cross section and pressure broadening and shift measurements were performed at a temperature of 700 ± 10 K in the central interaction region (the middle 20 cm of the vapor cell heated by a ceramic beaded heater (NiChrome V from Cole-Parmer) – see Fig. 3.2), corresponding to an average Yb density of ~ 5×10^{12} atoms/cm^3 in the interaction

region. The temperature of the central region is measured with a thermocouple and is consistent with that deduced from the observed Doppler width of Yb resonance lines. Fig. 3.3 shows the dependence of average Yb density on helium pressure at T_{cell} = 700 ± 10 K. The Yb density is found by measuring the absorption of 556 nm light, resonant with the $6s^2\ ^1S_0 \rightarrow 6s6p\ ^3P_1$ transition, passing through the vapor cell. The Yb density is determined from fits to the absorption profile.

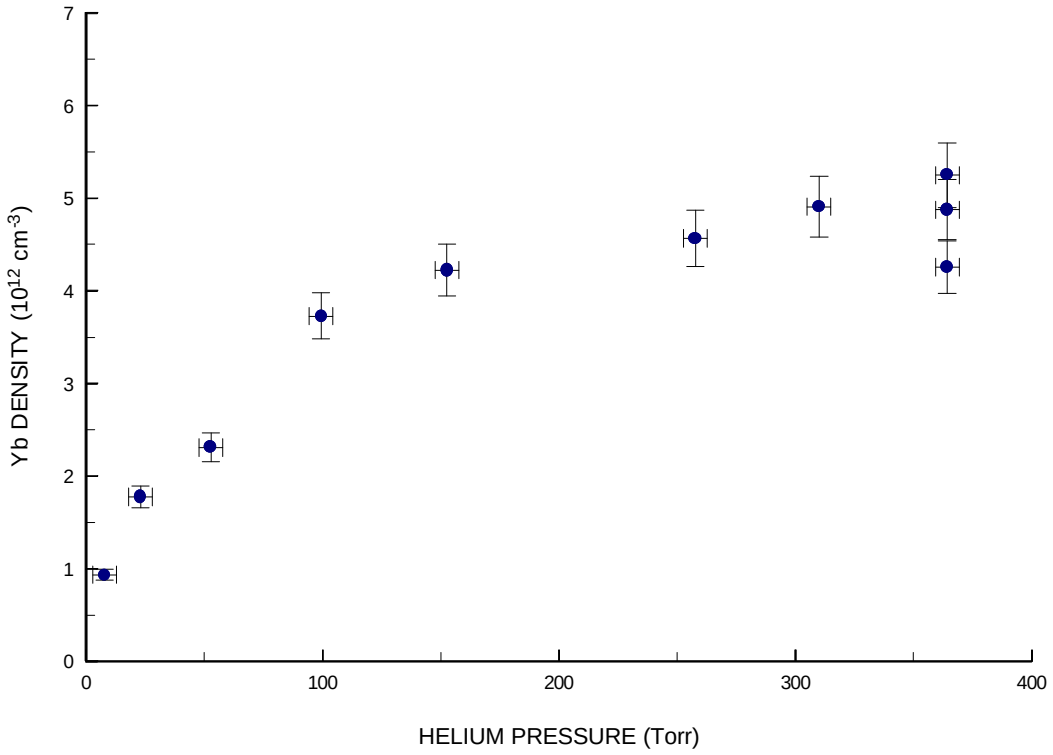

Figure 3.3 – *Average Yb density in the central interaction region with respect to helium pressure.*

Results for neon are similar. At buffer gas pressures less than 100 Torr, there is a strong dependence of Yb density on buffer gas pressure. Temperature measurements of the central region of the vapor cell (inside the tantalum liner) indicate that Yb density

variations are apparently related to a dependence of the temperature of the inner part of the cell on buffer gas pressure. This is probably caused by changes in thermal conductivity between the surface of the vapor cell and the tantalum liner when buffer gas density is varied. At low pressures, the tantalum liner is cooler than the outer walls of the cell. At pressures > 100 Torr, temperature variations are negligible. The Yb density is in agreement with the predicted Yb saturated vapor pressure [1].

Outside the interaction region ytterbium density falls rapidly – Yb condenses back to solid form within approximately 10 cm of the vapor cell center. The column length of ytterbium vapor is ≈ 15-20 cm, roughly matching the length of the heated central region of the vapor cell. Buffer gas pressure in the vapor cell is measured independently by two capacitance manometers (MKS Baratrons) – with ranges of 100 Torr and 5000 Torr.

The pulsed 262 nm pump beam is produced by an excimer (Lambda Physik EMG 101 MSC) pumped dye laser (Lambda Physik FL 2002) with frequency doubling. Coumarin 334 dissolved in methanol is employed as the laser dye to generate light at 524 nm. The 524 nm light passes through an angle-tuned BBO crystal producing second harmonic light at 262 nm. The laser system operates with a repetition rate of 5 Hz and each pulse at 262 nm has an energy of ~ 0.5 mJ, a duration of ~ 20 ns and a spectral width of ~ 0.5 cm^{-1}. The 262 nm pump beam passes through a lens that expands the beam diameter to ~ 1 cm in the central interaction region of the vapor cell. Due to the relatively broad spectral width of the 262 nm pump light, all isotopic and hyperfine components of the 6s6p $^3P_0$ state are populated.

The 649 nm probe light is generated by a home-made external cavity diode laser system. We use laser diodes with a nominal power of 20 mW [2]. The single frequency

output is typically 10 mW, tunable over approximately 3-5 GHz without mode hops or multimode behavior. The spectrum of the diode laser is monitored with a confocal scanning Fabry-Perot interferometer with a free spectral range (FSR) of 750 MHz and finesse of ≥ 50.

Most of the probe laser output is directed into a commercial Yb HCL filled with neon buffer gas. We use the optogalvanic signal to tune the probe laser to resonance with the 6s6p $^3P_0 \rightarrow$ 6s7s $^3S_1$ transition as discussed in Chapter Two. The HCL is connected to a constant voltage source through a balast resistor. A laser beam chopper provides modulation of the incident light, allowing observation of changes in the current through the HCL by monitoring the voltage across the resistor with a lock-in detector (PAR model 186). The diode laser probe beam is tuned to resonance with the even isotope components of the 6s6p $^3P_0 \rightarrow$ 6s7s $^3S_1$ transition by finding the largest peak near 649 nm.

Before entering the vapor cell, the probe beam passes through an iris which reduces the beam diameter to ~ 1 mm. The power of the probe beam (after the iris) is attenuated with filters to < 1 μW. We find that at this laser intensity the probe beam does not significantly affect the population of the metastable 6s6p $^3P_0$ state in comparison to other loss mechanisms. Loss rates from the 6s6p $^3P_0$ state with respect to helium density at two different laser powers are shown in Fig. 3.4, indicating optical pumping does not significantly effect $^3P_0$ population. This is consistent with the saturation parameter, which can be estimated as follows:

The optical pumping rate Γ_{pump} from the $^3P_0$ state is given by:

$$\Gamma_{pump} = \frac{d^2 E^2}{\Gamma_0} \frac{\Gamma_0}{g_D} = \frac{d^2 E^2}{g_D}, \tag{3.1}$$

where d is the dipole moment between the $^3P_0$ state and the $^3S_1$ state, E is the amplitude of the electric field for light at 649 nm, Γ_0 is the natural width of the $^3S_1$ state, and g_D is the Doppler width. The most important mechanism for replenishing the $^3P_0$ state population in the probe region is diffusion of excited Yb atoms from the pump region to the probe region (Γ_{d1} in Fig. 3.5). Thus we find the saturation parameter is given by:

$$S = \frac{\Gamma_{pump}}{\Gamma_{d1}} = \frac{d^2 E^2}{g_D \Gamma_{d1}} \tag{3.2}$$

Under typical conditions, the Doppler width is approximately $2\pi\cdot$(450 MHz) and the diffusion rate between the pump and probe region $\Gamma_{d1} \approx 2\times10^4$ s^{-1} (determined by fits to the diffusion rate from the pump region (Γ_{d2} in Fig. 3.5) and adjusting the parameter for the smaller diameter of the probe region). This yields $S \approx 0.1$, so under our conditions optical pumping can be ignored.

The probe and pump beams are aligned to propagate collinearly down the axis of the vapor cell, the smaller probe beam centered inside the larger pump beam (Fig 3.5). This geometry ensures that at sufficient buffer gas pressures atoms in the metastable $^3P_0$ state diffuse out of the pump region more slowly than they are quenched by collisions (i.e. the loss rate significantly exceeds the diffusion rate *from the pump region* $\Gamma_{loss} >> \Gamma_{d2}$).

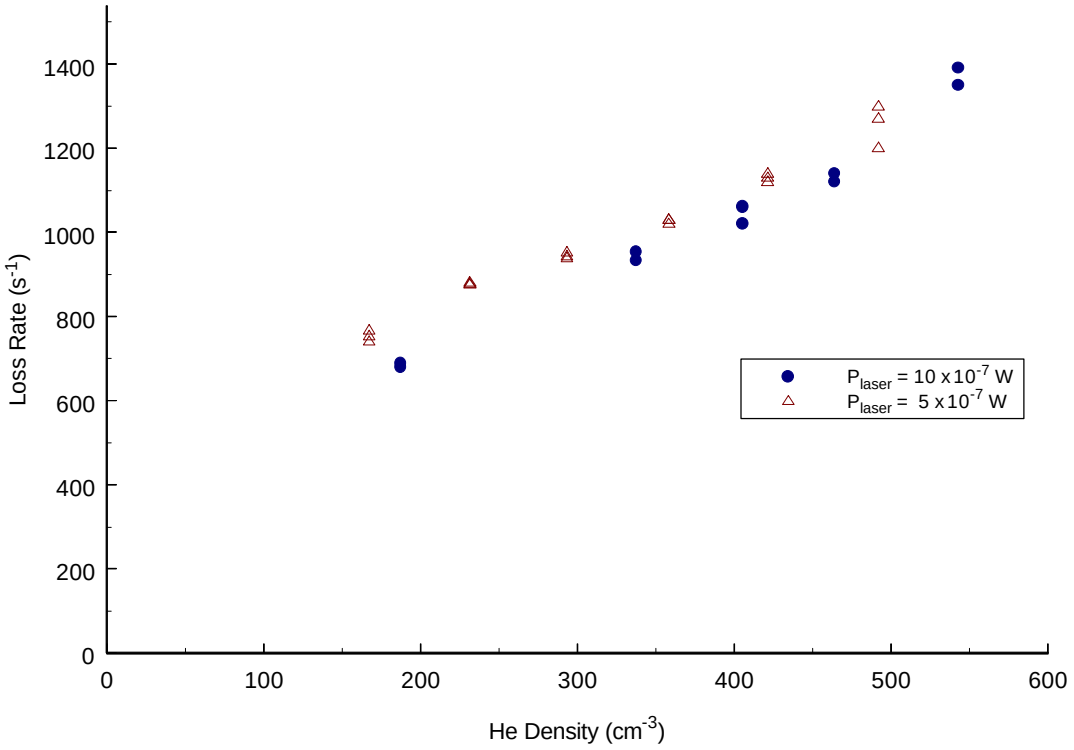

Figure 3.4 – *Loss rates from 6s6p $^3P_0$ state at two different laser powers, cell temperature is 700 K. There is no indication of optical pumping effects.*

We verify experimentally that slight misalignment of the beams has no discernible effect on measured cross section values nor on pressure broadening and shift values.

The 262 nm pump beam is retro-reflected by a dichroic mirror as it exits the cell, while the 649 nm probe beam is transmitted. The probe beam intensity after the cell is measured by a photodiode fitted with a 650 nm central wavelength interference filter with a 10 nm bandwith. The photodiode signal is captured on a Tektronix TDS 410A digital oscilloscope. The time dependence of the intensity is recorded individually for each pulse and sent to a computer running *Labview*™ data acquisition software. The time dependent intensity of 649 nm light at the photodiode determines the absorption at this

wavelength, which is a measure of the population of the Yb atoms in the 6s6p $^3P_0$ state within the probe region.

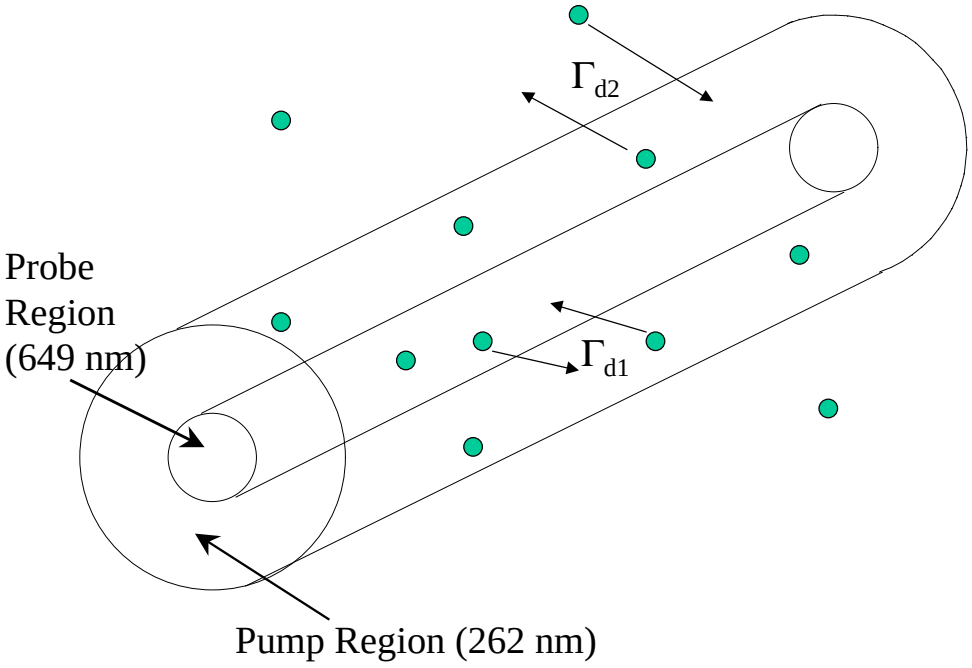

Figure 3.5 – *Illustration of the two relevant diffusion rates in our setup.* Γ_{d1} *is the diffusion rate of atoms between the pump and probe regions and* Γ_{d2} *is the diffusion rate of atoms from the pump region. Since the diameter of the probe region is smaller than the diameter of the pump region by a factor of ten,* $\Gamma_{d1} \approx 100\Gamma_{d2}$.

B. ***Absorption Profile***

The intensity of light $I(w,t)$ transmitted through the ytterbium vapor cell is described by:

$$I(w,t) = I_0(w)e^{-a(w,t)l}, \tag{3.3}$$

where $I_0(w)$ is the light intensity before the vapor cell, $l \approx 20$ cm is the length of the interaction region and $a(w,t)$ is the absorption coefficient, given by:

$$a(w,t) = \frac{3pc^2 n(t)}{w_0{}^3 t} \frac{w}{g_D} V(w) = a(w,0) \frac{n(t)}{n(0)}, \qquad (3.4)$$

where $n(t)$ is the density of Yb atoms in the lower state of a given transition within the probe region as a function of time, w_0 is the resonance frequency of the transition, w is the frequency of the probe laser, t is the lifetime of the upper state (t = 15(2) ns for the 6s7s $^3S_1$ state [3-5], and t = 872(2) ns [6] for the 6s6p $^3P_1$ state), g_D is the Doppler width and $V(w)$ is the Voigt lineshape function ($V(w)$ includes relative intensities of hyperfine components and isotopic abundance).

Thus a measurement of the intensity of light transmitted through the vapor cell directly determines the density of Yb atoms in the 6s6p $^3P_0$ state within the probe region as a function of time (note that self-broadening was found to be insignificant, as discussed below). There exist four primary mechanisms by which Yb atoms in the 6s6p $^3P_0$ metastable state are lost from the probe region: collisional de-excitation by buffer gas atoms, self-quenching, quenching by possible gaseous impurities and diffusion out of the probe region. Due to the distinct dependencies of these mechanisms on experimental parameters such as buffer gas pressure and cell temperature, we are able to distinguish between some of these various loss mechanisms.

The diffusion rate of Yb atoms in the 6s6p $^3P_0$ metastable state from the probe region decreases as buffer gas density is increased. Therefore by operating at sufficiently high buffer gas pressure (≥ 100 Torr) diffusion becomes negligible. Since collisional

quenching rates increase with perturber density, it is straightforward to distinguish collisional quenching from diffusion.

Since we are in the regime of low perturber density ($s^{1/2} < n^{-1/3}$), we may restrict ourselves to two-body collisions and apply the impact approximation [7]. The time dependence of the population of the 6s6p $^3P_0$ state is given by:

$$\frac{dn}{dt} \cong -\Gamma_{total} n \cong -\left(\Gamma_{quench-B} + \Gamma_{quench-Yb} + \Gamma_{quench-I}\right) n \,. \tag{3.5}$$

Therefore

$$n(t) = n_0 e^{-\Gamma_{total} t} \,, \tag{3.6}$$

where $n_0 \approx 10^{11}$ cm^{-3} is the initial density of Yb atoms in the 6s6p $^3P_0$ state after excitation by the 262 nm pump pulse, Γ_{total} is the total rate of loss of Yb atoms in the 6s6p $^3P_0$ state from the probe region, $\Gamma_{quench\text{-}B}$ is the quenching rate due to buffer gas collisions, $\Gamma_{quench\text{-}Yb}$ is the quenching rate due to collisions with Yb atoms and $\Gamma_{quench\text{-}I}$ is the quenching rate due to collisions with residual impurities in the cell. Under typical experimental conditions, the sum of the quenching rates due to Yb atoms and/or possible gaseous impurities is ~ 300-500 s^{-1} (determined from extrapolated quenching rates at zero buffer gas pressure). The quenching rate with respect to the buffer gas $\Gamma_{quench\text{-}B}$ depends linearly on the buffer gas density n_{buffer}:

$$\Gamma_{quench-B} = n_{buffer} \cdot s_{Yb-B} \cdot \bar{v}_{rel} \,, \tag{3.7}$$

where s_{Yb-B} is the collisional de-excitation cross section of the 6s6p $^3P_0$ state with respect to the buffer gas atoms and

$$\bar{v}_{rel} = \left(\frac{8k_B T}{pm}\right)^{1/2} \tag{3.8}$$

is the average relative velocity between Yb atoms and buffer gas atoms in their center of mass frame (m is the reduced mass of the Yb buffer gas atom system) . If ytterbium and impurity densities in the vapor cell are independent of buffer gas pressure, $\Gamma_{quench\text{-}Yb}$ and $\Gamma_{quench\text{-}I}$ are independent of buffer gas pressure (described by equations similar to (3.7), with n_{buffer} and s_{Yb-B} replaced with the appropriate quantities).

The normalized Voigt lineshape function $V(w)$ in equation (3.4) is given by [8]:

$$V(w) = \sum_i C_i g\left(z_i(w)\right), \tag{3.9}$$

where the index *i* refers to various isotopic and hyperfine components, the C_i's are constants which account for the isotopic abundance and relative intensity of particular hyperfine components and

$$g\left(z_i(w)\right) = \mathrm{Re}\left(\sqrt{p}\cdot\exp\left[-z_i(w)^2\right]\cdot\left(1-\Phi\left[-iz_i(w)\right]\right)\right). \tag{3.10}$$

$\Phi[x]$ is the complex error function [25] and

$$z_i(w) = \frac{w-w_i}{g_D} + i\left(\frac{g_N + g_P}{2g_D}\right), \tag{3.11}$$

w_i being the resonance frequency of a particular isotopic or hyperfine component, g_N is the natural width and g_P is the pressure width. Thus determination of the absorption coefficient as a function of probe laser detuning allows us to extract the Doppler and pressure widths. We assume *a priori* the separation of the hyperfine and isotope components and their relative intensities as measured by others [9-14]. We also assume that all hyperfine components experience the same broadening and shift.

Self-broadening could mimic a change in $^3P_0$ population by causing $V(w)$ to acquire a time dependence, since $g_P(self) \propto n(t)$. Pressure widths at different cell

temperatures (where Yb density varied by over an order of magnitude) were measured and agreed within uncertainty. This indicates that the effects of self-broadening are negligible for our purposes.

C. *6s6p $^3P_0$ Quenching Cross Sections*

Yb atoms excited from the ground state to the 6s7p $^3P_1$ state by the 262 nm pump beam populate the 6s6p $^3P_0$ state via cascade decay within ~ 150 ns. Once the 6s6p $^3P_0$ state is populated, the medium is no longer transparent to the 649 nm probe beam. The intensity of light at 649 nm transmitted through the vapor cell is described by equation (3.1). The photodiode detector circuit which monitors 649 nm intensity after the cell has a finite response time t_r ~ 30 μsec. At times *t* much longer than t_r the voltage signal $j(t)$ from the photodiode is:

$$j(t) = B_0 \exp[-A\exp[-\Gamma t]], \tag{3.12}$$

where B_0 is the initial photodiode signal amplitude due to incident light, A is the absorption coefficient just after the excitation pulse at t = 0 ($a(w,0)$ from equation (3.4)) times length of the interaction region *l*, and Γ is the total loss rate of Yb atoms in the 6s6p $^3P_0$ state from the probe region. For each pulse the experimental signal is saved to computer and fit to equation (3.12). Analysis yields values for the total loss rate Γ and the absorption coefficient $a(w,t)$. A fit to typical data is shown in Fig. 3.6.

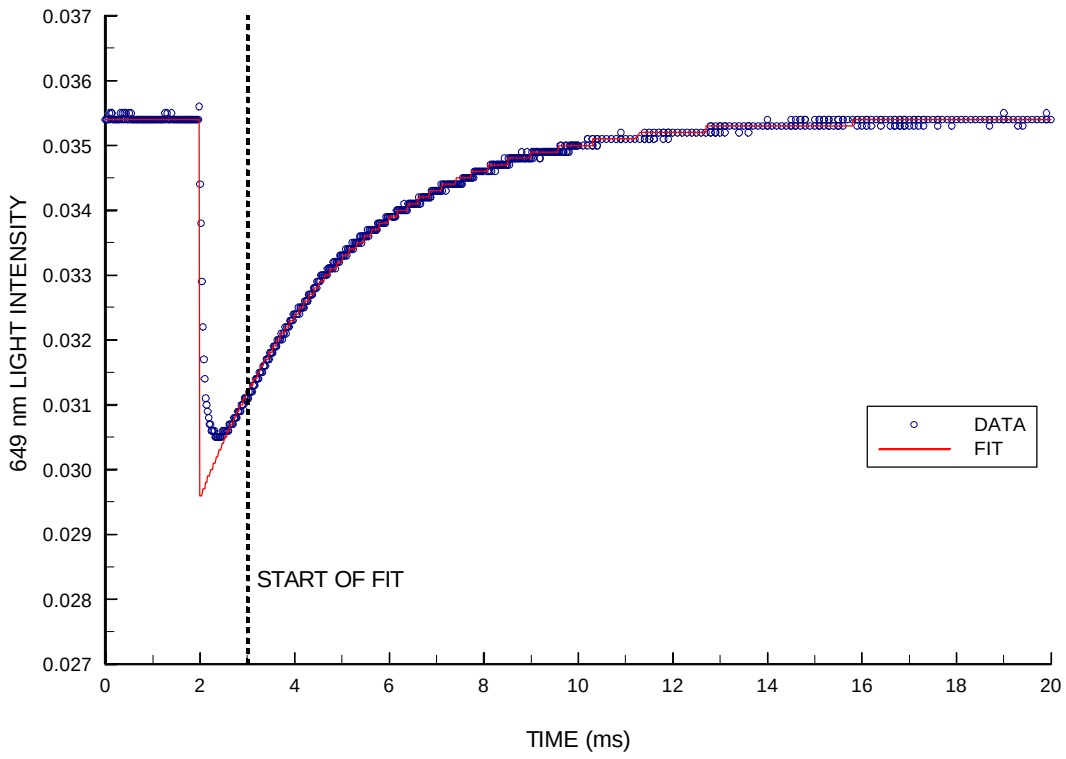

Figure 3.6 – *Intensity of 649 nm light transmitted through the vapor cell. This particular data set is with neon buffer gas at a pressure of 100 Torr. The 262 nm pulse passes through the vapor cell at t = 2 ms, populating the 6s6p $^3P_0$ state. The fit is performed with data after t = 3 ms where the photodiode circuit response effects (evident for times between 2.0 and 2.5 ms) have died away.*

Data are taken at buffer gas pressures ranging from 100 to 600 Torr. At higher pressures, collisional broadening of the probe transition reduces the signal to noise ratio to unacceptable levels. Below ~ 100 Torr, diffusion effects dominate over collisional quenching of the 6s6p $^3P_0$ state and Yb density has a strong dependence on buffer gas pressure (Fig. 3.3). Fig. 3.7 shows the total loss rate Γ with respect to helium and neon densities for buffer gas pressures between 100 and 600 Torr. Each data point is the average of results from four to eight pump laser pulses.

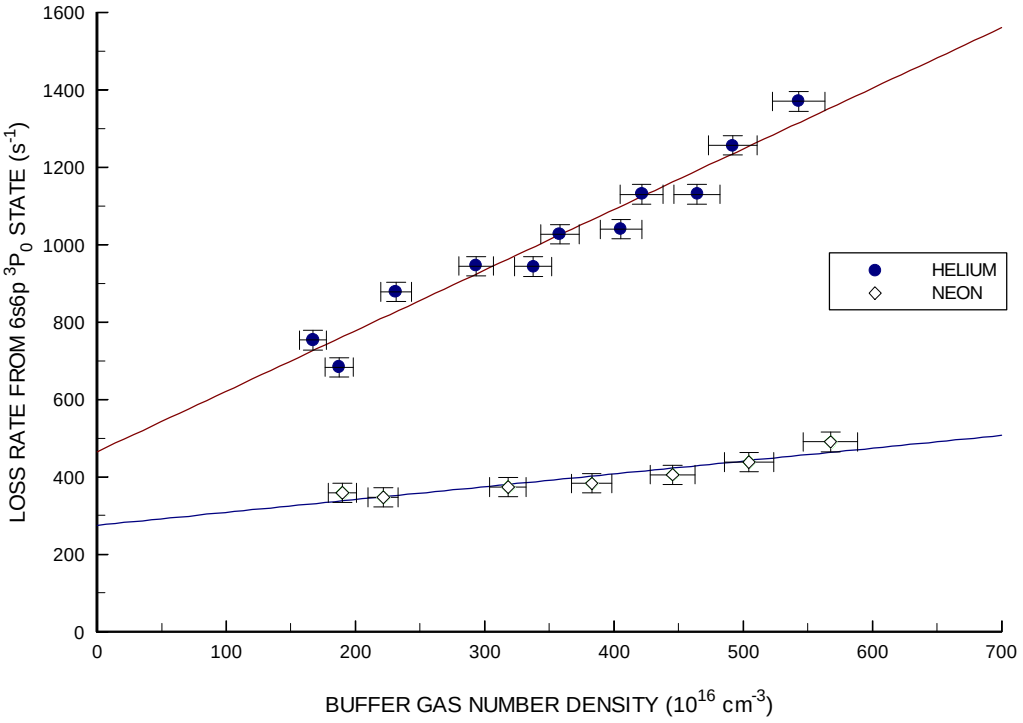

Figure 3.7 – *Total loss rate G of Yb atoms in the 6s6p $^3P_0$ state from the probe region with respect to buffer gas density. Each data point is the average of 4-8 laser pulses. The straight lines are least squares fits. The difference between the y-intercepts of the two data sets is consistent with variations in ytterbium density between runs.*

The linear dependence of Γ on buffer gas density provides an upper limit for the 6s6p $^3P_0$ quenching rate due to collisions with buffer gas atoms (equation (3.7)). Sources of uncertainty in the measurements of quenching rates at different buffer gas pressures and their contribution to the uncertainty in $s_{Yb-B} \cdot \bar{v}_{rel}$ are summarized in Table 4.

Table 4: Sources of uncertainty in determination of $s_{Yb-B} \cdot \bar{v}_{rel}$.

	Contribution to uncertainty in $\langle\sigma v\rangle$ (10^{-17} cm^3/s)	
SOURCE OF UNCERTAINTY	**HELIUM**	**NEON**
Uncertainty in buffer gas density	1.4	0.3
Change in Γ with start of fit	8.0	1.3
Variation of Yb density with buffer gas pressure	2.0	2.0
Statistical uncertainty	1.0	0.4
TOTAL	**8.4**	**2.4**

Due to the small quenching cross sections with respect to buffer gas atoms ($s_{Yb-B} \lesssim 10^{-21}$ cm^2), a slight dependence of Yb or impurity density on buffer gas density may be the primary cause of the linear dependencies observed in Fig. 3.6. Based on quenching rate measurements at different cell temperatures, we estimate the Yb-Yb quenching cross sections (for both ground and excited states) s_{Yb-Yb} to be ~ 10^{-14} cm^2 (Figs. 3.8, 3.9). The measurement of Yb density variations with respect to buffer gas pressure at fixed cell temperature (Fig. 3.3) provides a limit on the uncertainty in $s_{Yb-B} \cdot \bar{v}_{rel}$ from Yb-Yb quenching, $d\left(s_{Yb-B}\bar{v}_{rel}\right)_{Yb-Yb}$:

$$d\left(s_{Yb-B}\bar{v}_{rel}\right)_{Yb-Yb} \leq \frac{\Delta n_{Yb} s_{Yb-Yb} \cdot \bar{v}_{rel}}{\Delta n_{buffer}}, \tag{3.13}$$

where Δn_{Yb} is the change in Yb density for a given change in buffer gas pressure Δn_{buffer}.

Although the measurements for He and Ne were performed nominally at the same vapor cell temperature (700 K), the total Yb density probably differed between runs due to slight temperature differences ($\Delta T \approx 10$ K).

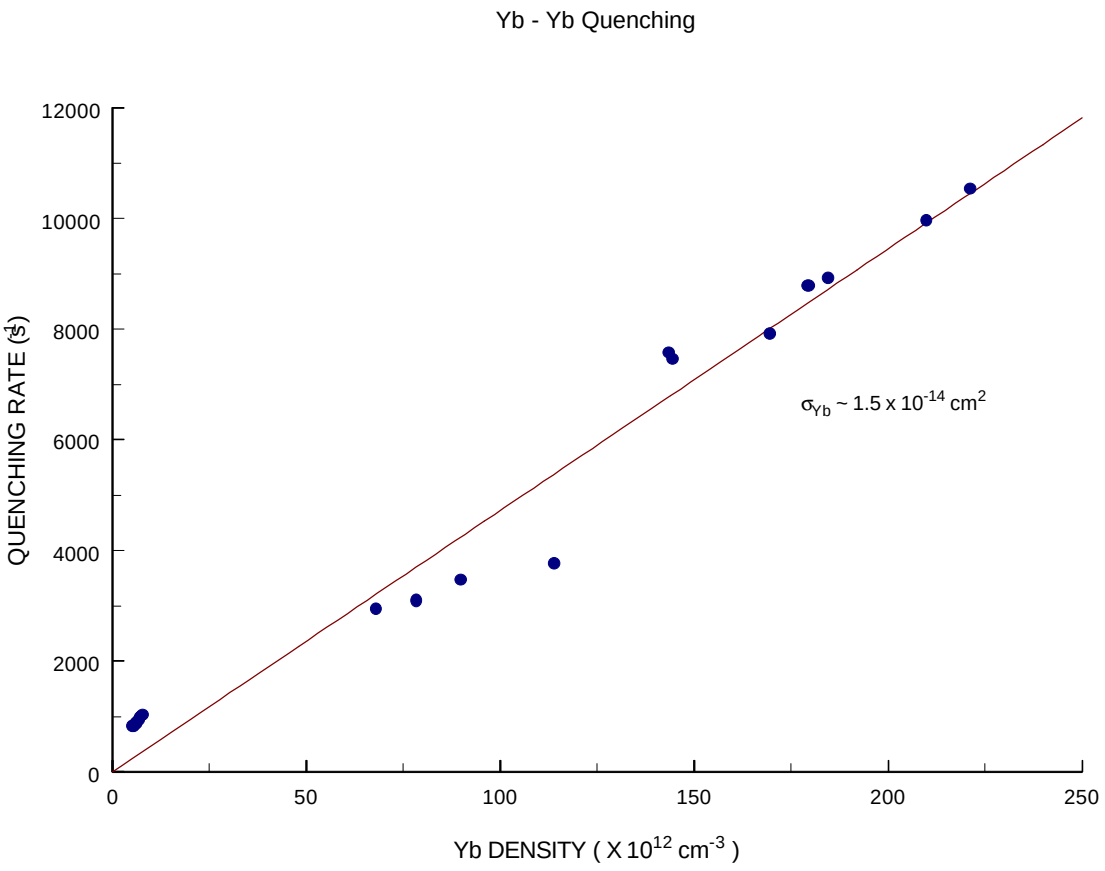

Figure 3.8 – *Total loss rate of Yb atoms in the 6s6p $^3P_0$ state from the probe region with respect to total Yb density. The Yb density is varied by changing the cell temperature.*

Hence, a relatively small difference in Yb density (~ 10^{12} cm^{-3}) can explain the observed difference between the extrapolated quenching rates at zero buffer gas pressure for He and Ne in Fig. 3.7.

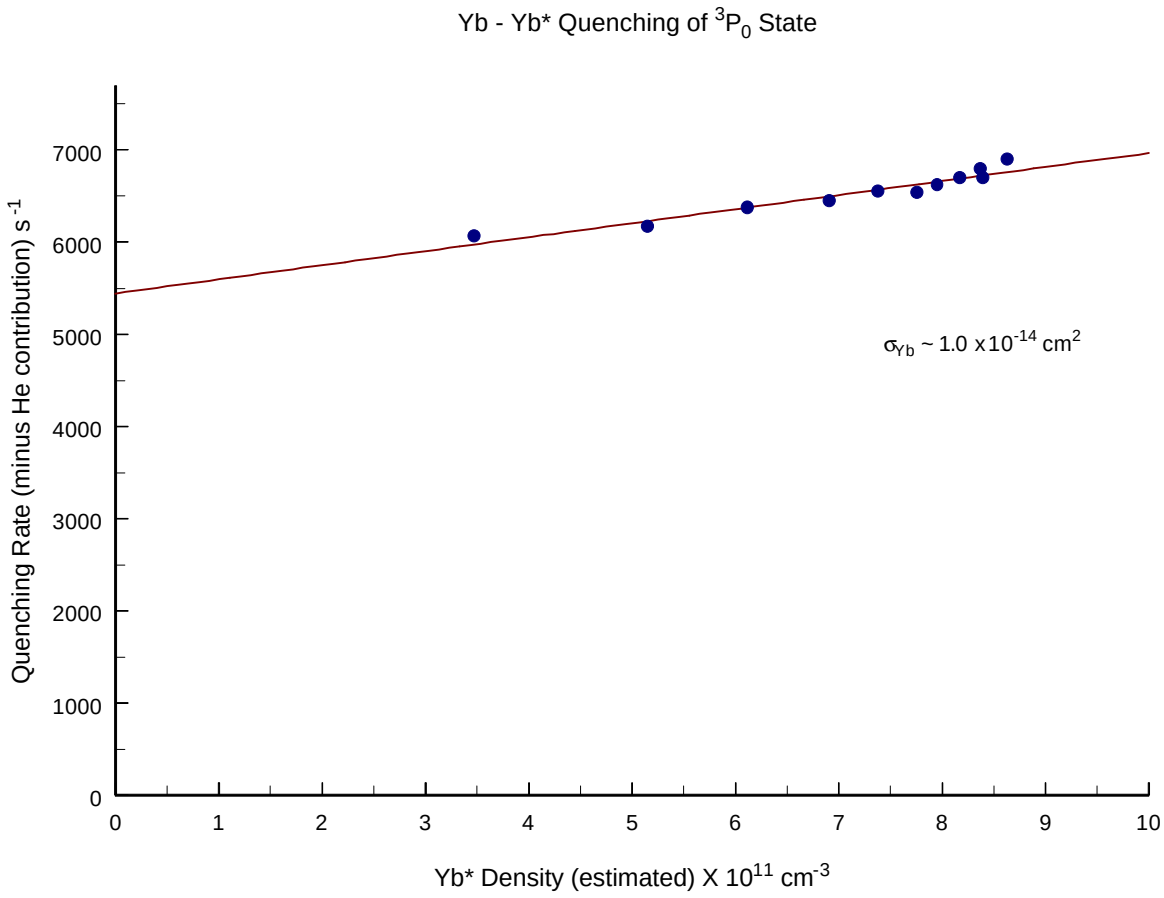

Figure 3.9 – *Total loss rate of Yb atoms in the 6s6p $^3P_0$ state from the probe region with respect to estimated excited state Yb density (from pump laser power and branching ratio estimates).*

There may also be impurities with high cross sections in the cell. Since the cell is pumped down to 10^{-2} Torr, we estimate that the impurity density in the cell could be as large as 10^{14} cm^{-3}. However, adding more inert buffer gas should not decrease the impurity density, and pumping buffer gas out of the cell should not increase the impurity density. So it is reasonable to assume that impurities in the cell can only add to the measured value of $s_{quench-B} \cdot \bar{v}_{rel}$. Therefore, the measured quenching cross sections can

be interpreted as upper limits on the values of the true quenching cross sections with respect to He and Ne.

Buffer gas density was calculated from the ideal gas law based on the measured pressure and temperature in the interaction region. Hence, uncertainties in buffer gas pressure and cell temperature lead to an uncertainty in buffer gas density.

An additional systematic uncertainty arises from a slight dependence of the value of Γ on the start time of the fit, indicating that equation (3.12) does not perfectly describe our data. This discrepancy may be attributed to a non-uniform Yb density distribution within the probe region due to the temperature gradient between the center and edges of the central part of the cell. This can affect both $a(w,t)$ and $\Gamma_{quench\text{-}Yb}$, leading to a more complicated time dependence of the transmitted light intensity than assumed in equation (3.9). In order to illustrate the nature of these effects, we suppose that some fraction *x* of the Yb atoms near the edge of the interaction region experience a smaller Yb density (suppose Yb density is $n_{Yb}^{(1)}$ at the center and $n_{Yb}^{(2)}$ near the edge). Under these conditions, the 6s6p $^3P_0$ population as a function of time is given by:

$$n(t) = (1-x)n_0 e^{-\Gamma_1 t} + x n_0 e^{-\Gamma_2 t}\,. \tag{3.14}$$

Now we have two distinct quenching rates:

$$\Gamma_1 = \Gamma_{quench-B} + (1-x)n_{Yb}^{(1)} s_{quench-Yb} v_{Yb-Yb} + \Gamma_{quench-I} \tag{3.15}$$

and

$$\Gamma_1 = \Gamma_{quench-B} + x \cdot n_{Yb}^{(2)} s_{quench-Yb} v_{Yb-Yb} + \Gamma_{quench-I}\,. \tag{3.16}$$

If we fit fake data based on two quenching rates with a formula assuming a single quenching rate Γ_{total}, we find that Γ_{total} changes depending on the start of the fit and is

bounded between Γ_1 and Γ_2. In the actual experiment, there is a continuous density and quenching rate distribution leading to a more convolved, but essentially similar, expression. Experimentally, the change in the quenching rate with the start of the fit is relatively small (~5%), however, so we include it as an uncertainty in the cross section values.

Considering these uncertainties, we conclude that:

$$s_{Yb-He} \cdot \bar{v}_{rel} < 26 \times 10^{-17} \text{ cm}^3/\text{s}$$

$$s_{Yb-Ne} \cdot \bar{v}_{rel} < 8 \times 10^{-17} \text{ cm}^3/\text{s}.$$

From equation (3.8) the average relative velocity between Yb and buffer gas atoms is:

$$\bar{v}_{rel}(He-Yb) = 1.950(14) \times 10^5 \text{ cm/s}$$

$$\bar{v}_{rel}(Ne-Yb) = 1.070(8) \times 10^5 \text{ cm/s}.$$

So we find that the average quenching cross sections are:

$$s_{Yb-He} < 13 \times 10^{-22} \text{ cm}^2$$

$$s_{Yb-Ne} < 8 \times 10^{-22} \text{ cm}^2.$$

D. *Pressure Broadening and Shift of the 6s6p $^3P_0$ ® 6s7s $^3S_1$ Transition*

Varying the frequency of the 649 nm probe light allows us to determine the lineshape of the 6s6p $^3P_0 \rightarrow$ 6s7s $^3S_1$ transition at various buffer gas pressures (Fig. 1.5). The intensity of 649 nm light transmitted through the vapor cell is measured at a fixed time after the pump pulse at 262 nm populates the 6s6p $^3P_0$ state. We fit the data to equation (3.3) using the frequency dependent absorption coefficient, equation (3.4), and extract the pressure width from the normalized Voigt profile, equations (3.9-3.11). Comparison with the simultaneously recorded optogalvanic signal from the Yb HCL allows us to determine the relative pressure shift. A typical data set is shown in Fig. 3.10.

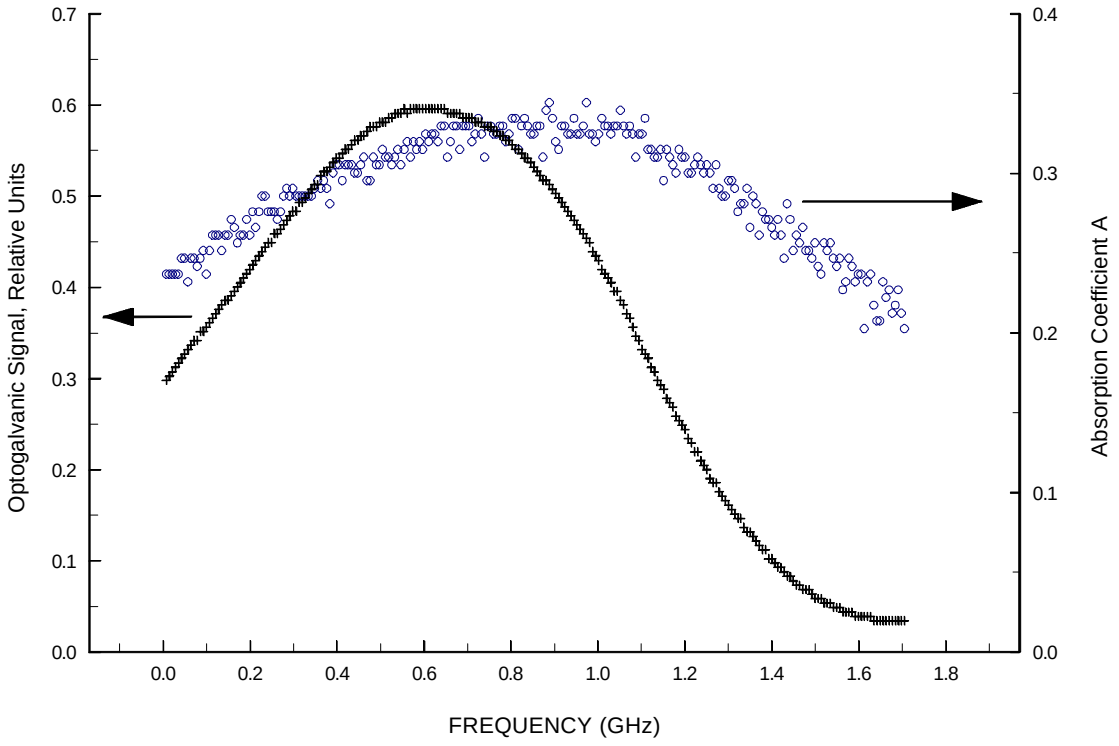

Figure 3.10 – *Typical data for measurement of pressure broadening and shift of the 649 nm 6s6p $^3P_0$ ® 6s7s $^3S_1$ transition. This data set was taken at a helium pressure of 70 Torr.*

The Doppler width is determined by fits to data at low buffer gas pressure ($\precsim$ 1 Torr), and is in agreement with the observed temperature in the central region of the vapor cell. Fits to a Voigt profile with the Doppler width held constant determine the width due to collisional broadening. Pressure shift and total width at various helium and neon pressures is plotted in Fig. 3.11, and the results for the pressure broadening and shift

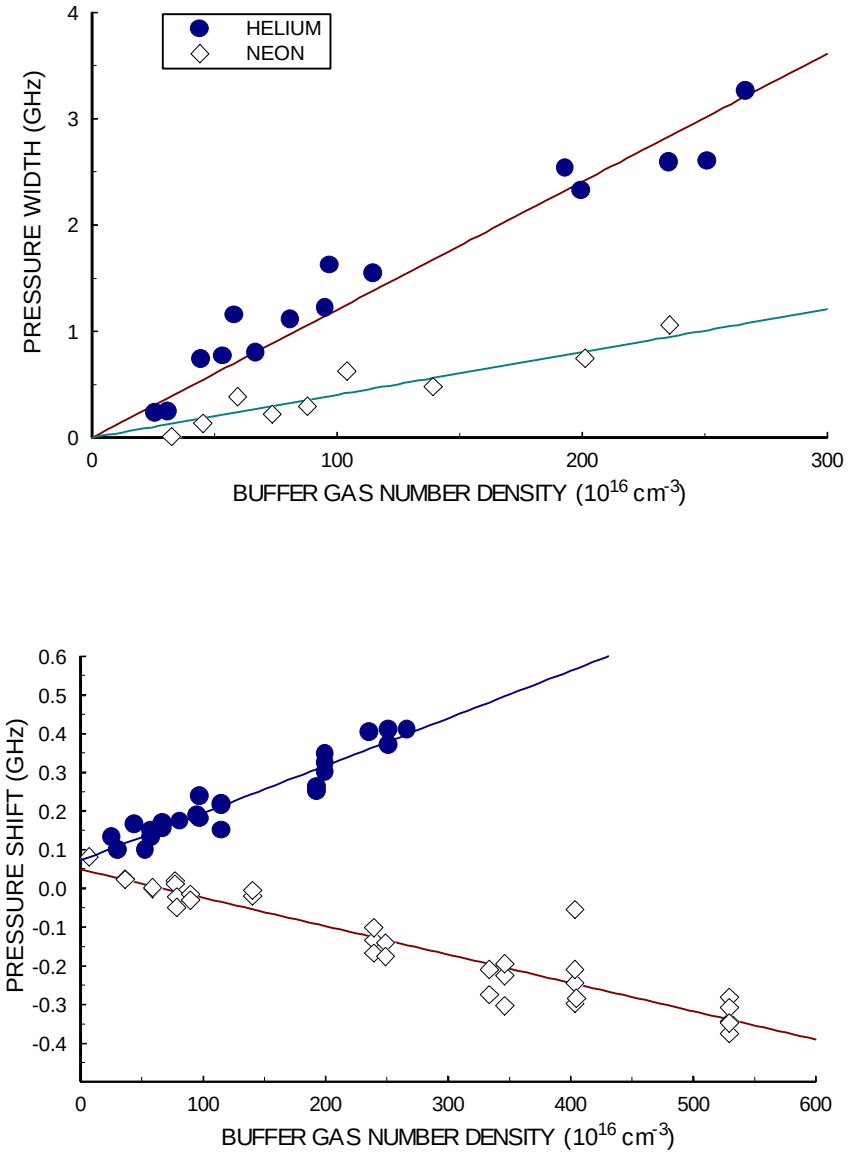

Figure 3.11 – *Pressure broadening and shift of the 649 nm 6s6p $^3P_0$ ® 6s7s $^3S_1$ transition by helium and neon.*

of the 6s6p $^3P_0 \rightarrow$ 6s7s $^3S_1$ transition are given in Table 5. Systematic uncertainties due to laser frequency scan nonlinearity, occasional mode hops, multimode behavior and uncertainties in the vapor cell temperature and buffer gas pressure were found to be on the order of the statistical spread of the points. Possible gaseous impurities in the cell do not significantly affect these measurements since broadening and shift cross sections are of the usual size (10^{-15} to 10^{-14} cm^2) while impurity density is relatively low.

Table 5: Pressure Broadening and Shift Rates for the 6s6p $^3P_0 \rightarrow$ 6s7s $^3S_1$ Transition (Γ / n) in units of 10^{-9}s^{-1}cm^3.

	Broadening	Shift
HELIUM	7.5 ± 1.3	0.8 ± 0.1
NEON	2.5 ± 0.3	-0.5 ± 0.1

The fits in Fig. 3.11 indicate there is a non-zero shift at low buffer gas pressure. Since the central frequency of the resonance is determined from fits to the optogalvanic signal, this shift is probably due to collisions in the discharge. The hollow cathode lamp contains about 20 Torr of neon, so the observed shift is consistent with that due to Ne in the HCL.

CHAPTER FOUR: Pressure Broadening and Shift of the $6s^2\ {}^1S_0 \rightarrow 6s6p\ {}^3P_1$ Transition

A. *Experimental Setup*

The pressure broadening and shift of the 556 nm $6s^2\ {}^1S_0 \rightarrow 6s6p\ {}^3P_1$ transition is determined by comparing the absorption spectrum in the vapor cell and fluorescence of an effusive Yb atomic beam, using the apparatus depicted in Fig. 4.1.

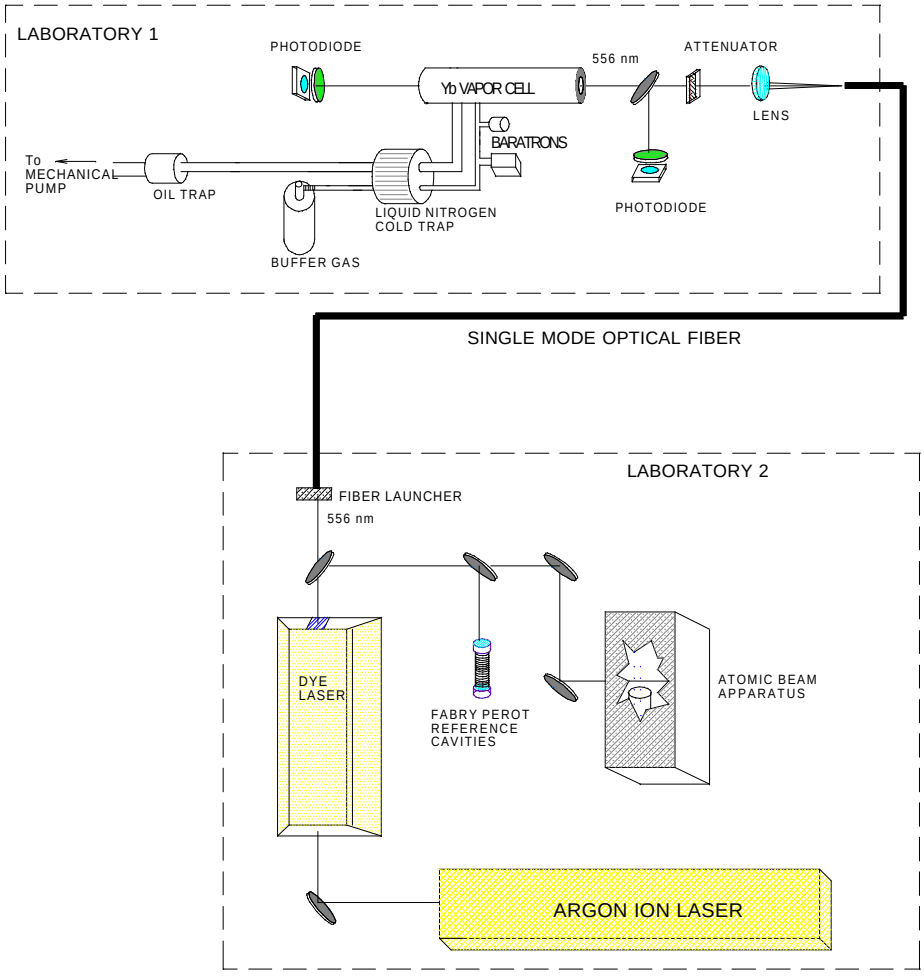

Figure 4.1 – *Experimental set-up for measurement of the 556 nm $6s^2\ {}^1S_0$ ® $6s6p\ {}^3P_1$ pressure broadening and shift.*

Light at 556 nm is generated by an Ar^+ laser pumped ring dye laser (Spectra-Physics 380D) using Rhodamine 110 (also known as Rhodamine 560 Chloride) dissolved in ethylene glycol. The atomic beam apparatus is essentially the same as that used in the previous work in this laboratory [1]. Light at 556 nm excites atoms in the atomic beam to the $6s6p\ ^3P_1$ state, and fluorescence at 556 nm is detected with a photomultiplier tube. A portion of the laser output is coupled into a single-mode optical fiber which takes the light into a different laboratory where measurements with the vapor cell are performed. Photodiodes monitor the intensity of incident light before and after passing through the cell. The power of the light passing through the vapor cell is attenuated to less than 500 nW, far from saturation of the transition. The laser is scanned through 20 GHz to measure the lineshape of the transition in the atomic beam and in the vapor cell. For high Yb densities and high buffer gas pressures – when the lines in the vapor cell become broad – it is necessary to concatenate multiple scans to accurately determine both the shape of the wings and the position of the line center. Frequency markers from two Fabry-Perot interferometers (FSR 500 MHz and FSR 10 GHz) and isotope shifts and hyperfine structure of the $6s^2\ ^1S_0 \rightarrow 6s6p\ ^3P_1$ transition allow us independent ways to calibrate the frequency scans of the laser.

B. ***Results***

The intensity of 556 nm light transmitted through the vapor cell is described by equation (3.3), except that in this case the absorption coefficient is time independent. Data is fit to equation (3.3) and the pressure broadening is extracted from the parameters of the best fit to a Voigt profile. The pressure shift is determined by comparing the 556

nm fluorescence from the atomic beam to absorption in the vapor cell. Fig. 4.2 shows typical absorption profiles at various buffer gas pressures compared to fluorescence from the atomic beam.

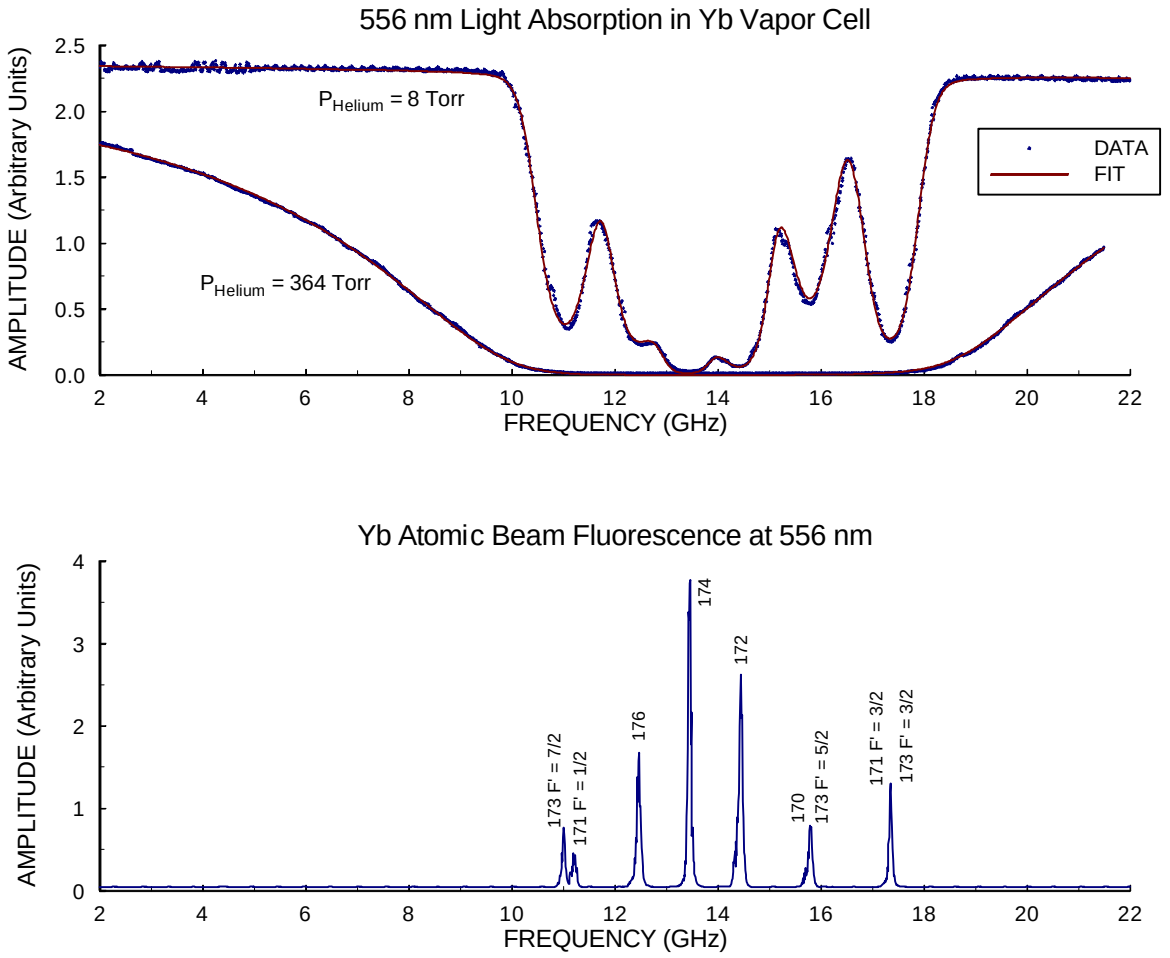

Figure 4.2 – *Typical data for measurement of the pressure broadening and shift of the 556 nm $6s^2\ {}^1S_0$ ® $6s6p\ {}^3P_1$ transition. For atomic beam fluorescence data, isotopic components are labeled with the respective atomic masses. F' is the total angular momentum of the upper state a hyperfine transition.*

As one can see from Fig. 4.2, at low pressures the hyperfine structure and isotope shifts are partially resolved while at higher pressures the absorption profile becomes relatively featureless. Fig. 4.3 shows a plot of the pressure broadening at various helium and neon pressures. The results are presented in Table 6. The scatter of shift data is relatively

large due to the difficulty in absolute frequency calibration of the featureless absorption profile at high buffer gas density. Least squares fits give shifts consistent with zero for both helium and neon.

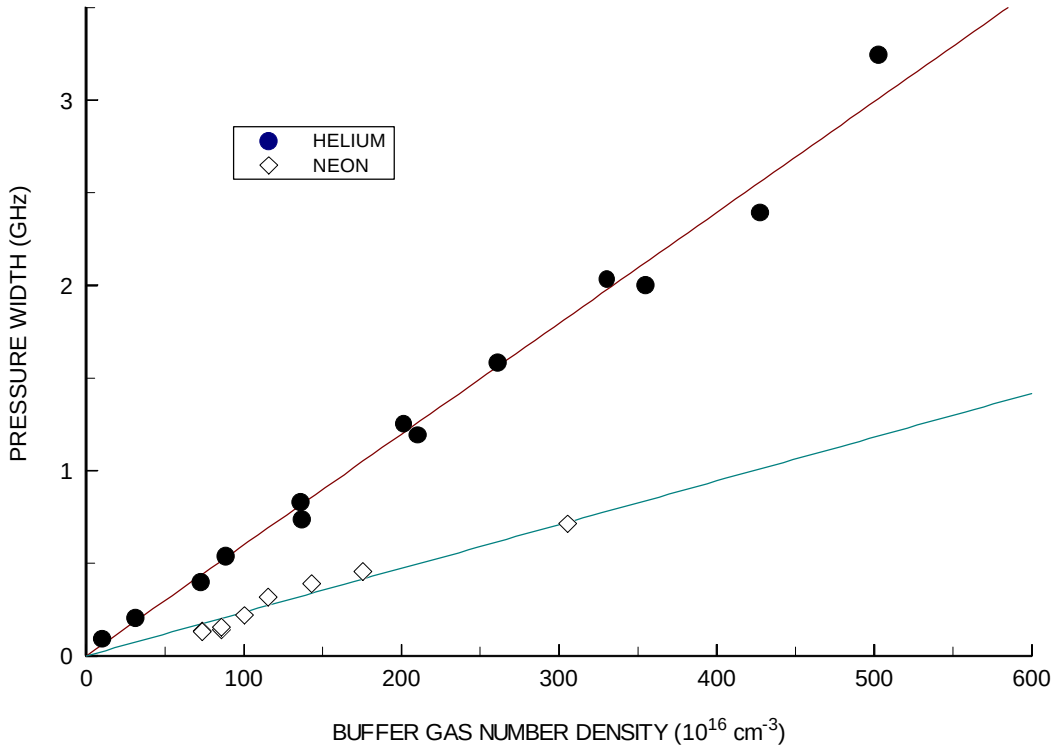

Figure 4.3 – *Pressure broadening of the 556 nm $6s^2\ ^1S_0$ ® $6s6p\ ^3P_1$ transition.*

Table 6: Pressure Broadening and Shift Rates for the $6s^2\ ^1S_0 \rightarrow 6s6p\ ^3P_1$ Transition (Γ / n) in units of $10^{-9}s^{-1}cm^3$.

	Broadening	Shift
HELIUM	3.8 ± 0.1	0.0 ± 0.5
NEON	1.5 ± 0.1	-0.5 ± 1.0

CHAPTER FIVE: Consequences for a Parity Nonconservation Experiment

The exceptionally small collisional de-excitation cross sections of the 6s6p $^3P_0$ state may make an Yb PNC experiment in a vapor cell advantageous. A possible configuration for such an experiment is shown in Fig. 5.1. Here one employs the PNC-Stark interference technique, where the observable is a difference in transition rates arising from the interference of Stark-induced and PNC-induced transition amplitudes for right- and left-handed experimental configurations. This geometry is similar to that of the currently most precise PNC experiment performed in a cesium atomic beam by the group in Boulder [1].

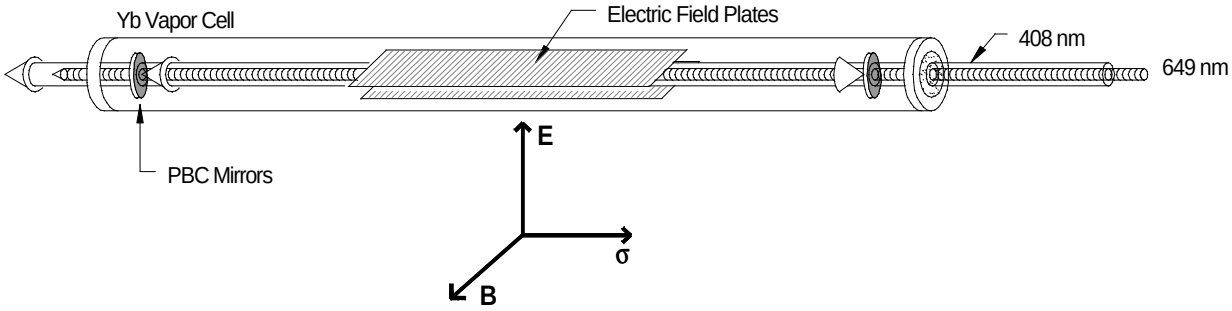

Figure 5.1 – *Schematic diagram of apparatus for proposed Yb PNC experiment in a vapor cell.*

The PNC-induced asymmetry corresponding to the pseudoscalar rotational invariant $\vec{s}\cdot\left(\vec{E}\times\vec{B}\right)$ would be measured by comparing how many Yb atoms are excited to the upper state of the 408 nm $6s^2\ ^1S_0 \rightarrow 6s5d\ ^3D_1$ transition for different orientations of $\vec{s}$ (angular momentum of excitation beam), $\vec{E}$ (static electric field), and $\vec{B}$ (static magnetic field). It is also possible to use a geometry similar to that used to study PNC in

thallium by the Berkeley group [2]. In this case the pseudoscalar invariant is $\left(\hat{e}\cdot\vec{B}\right)\left(\hat{e}\cdot\vec{E}\times\vec{B}\right)$ where $\hat{e}$ is the excitation light polarization. Such an arrangement suppresses systematic uncertainties associated with the $M1$ amplitude.

In an envisioned PNC experiment, Yb atoms will be excited to the 6s5d $^3D_1$ state by intense 408 nm light produced by directing continuous wave laser light into a multipass or power buildup cavity. Atoms excited to the 6s5d $^3D_1$ state subsequently decay to the 6s6p $^3P_0$ state. As in the present work, the 6s6p $^3P_0$ population will be monitored with a weak probe beam at 649 nm (Fig.1.1). Performing a parity violation measurement in a vapor cell offers a number of potential advantages compared to a similar experiment in an atomic beam. A vapor cell enables higher counting rates due to greater atomic densities and superior detection efficiency is achieved by measuring absorption of a probe laser as opposed to measuring fluorescence. As discussed in chapter 1, the high detection efficiency using absorption is only achieved for sufficiently dense ($l/l_0 \approx 2$) samples.

We conservatively estimate that the cavity inside the vapor cell should be able to achieve a gain of at least 500 (about 2 orders of magnitude less than that achieved by the Boulder group [1]). With an input power of ~ 200 mW, this is sufficient to produce ~ 100 W of power at 408 nm in the interaction region. Two absorption lengths at the probe transition, which permits the maximal detection efficiency, requires a density of ~ 10^{10} Yb atoms per cm^3 in the 6s6p $^3P_0$ state (for an interaction region of about 50 cm length). After pumping for a sufficiently long time:

$$n_{3P0} \approx \frac{\Gamma_{pump}}{\Gamma_{loss}} n_{total}, \tag{5.1}$$

where the pump rate Γ_{pump} (in s^{-1}, assuming a beam diameter of ~ 1mm) is given by:

$$\Gamma_{pump} \sim \frac{\left(|b| E_{stat} E_{408}\right)^2}{g_D} \sim 5\times 10^{-5} E_{stat}^2 , \tag{5.2}$$

E_{stat} being the static electric field, E_{408} being the electric field amplitude of the 408 nm light (in V/cm) and $|b| = 2.18(33) \times 10^{-8}\ ea_0/(\text{V/cm})$ is the vector transition polarizability [3]. Using neon as our buffer gas at a pressure of ~ 400 Torr at a cell temperature of around 700 K (yielding a total Yb density of 5×10^{12} atoms/cm^3), we find that the necessary static electric field in order to accumulate 2 absorption lengths for the probe transition is approximately 700 V/cm. Since the breakdown voltage for neon under these conditions is >> 700 V/cm [4], it appears this field amplitude is achievable in the proposed experimental configuration.

The fractional uncertainty in a measurement of $E1_{PNC}$ can be estimated to be:

$$\frac{d\,E1_{PNC}}{E1_{PNC}} \sim \frac{\sqrt{N_{total}}}{\Delta N_{PNC}}, \tag{5.3}$$

where N_{total} is the total number of atoms detected in the 6s6p $^3P_0$ state:

$$N_{total} \sim \frac{\left(|b| E_{stat} E_{408}\right)^2}{g_D} N_{Yb} T e_d \tag{5.4}$$

and ΔN_{PNC} is the difference in the total number of atoms detected in the 6s6p $^3P_0$ state between left and right handed configurations of experimental quantities (the asymmetry due to PNC-Stark interference), given by:

$$\Delta N_{PNC} \sim \frac{4|b| E_{stat} E_{408}^2 E1_{PNC}}{g_D} N_{Yb} T e_d , \tag{5.5}$$

where $E1_{PNC}$ is the PNC-induced $E1$ amplitude for the 408 nm transition, N_{Yb} is the total number of Yb atoms in the interaction region, T is the measurement time in seconds and e_d is the detection efficiency. This yields a fractional uncertainty in $E1_{PNC}$ of

$$\frac{d\,E1_{PNC}}{E1_{PNC}} \sim \frac{1}{\sqrt{T}}\left(\frac{1}{4E_{408}E1_{PNC}}\sqrt{\frac{g_D}{N_{Yb}e_d}}\right). \tag{5.6}$$

As is commonly the case in Stark-PNC interference experiments, there is no dependence on the static electric field.

Table 7: Estimated experimental parameters for Yb PNC experiment in a vapor cell and an atomic beam.

Parameter	***CELL***	***BEAM***
E_{408}	3 kV/cm	12 kV/cm
γ_D	$2\pi\cdot$1000 MHz	$2\pi\cdot$30 MHz
ε_d	1	0.1
N_{Yb}	2.5×10^{11} atoms	2×10^{8} atoms

We can now compare the statistical sensitivity of such an Yb PNC experiment performed in a vapor cell to a similar experiment in an Yb atomic beam. Based on estimates of experimental parameters from this work for a vapor cell and [3,5,6] for an atomic beam (presented in Table 7), we find from equation (5.6) the fractional uncertainties in $E1_{PNC}$ for a cell experiment and a beam experiment to be:

$$\left(\frac{dE1_{PNC}}{E1_{PNC}}\right)^2_{cell} \approx \frac{5\times10^{-6}}{T}$$

$$\left(\frac{dE1_{PNC}}{E1_{PNC}}\right)^2_{beam} \approx \frac{10^{-4}}{T}.$$

This demonstrates that an Yb vapor cell experiment may offer advantages in statistical sensitivity to PNC effects in comparison to an atomic beam experiment. However, it is also possible that other factors will be of greater importance in determining which method is best suited for a PNC experiment, since both techniques appear capable of achieving high statistical sensitivity.

There remain a number of open questions that need to be addressed before pursuing an Yb PNC experiment in a vapor cell. A possible complication arises due the Doppler and pressure widths of the 408 nm resonance in a vapor cell leading to overlap of isotope and hyperfine components of the $6s^2\ ^1S_0 \rightarrow 6s5d\ ^3D_1$ transition. This would make isotopic comparisons more difficult and would also require a larger magnetic field to separate the Zeeman components. The same difficulties exist for the 649 nm probe transition. Additionally, ionization of Yb atoms by the 408 nm light and collisionally assisted transitions to the upper state of the 408 nm $6s^2\ ^1S_0 \rightarrow 6s5d\ ^3D_1$ transition may be problematic. These questions will be addressed in future experimental work.

CONCLUSION

We have placed upper limits on the collisional quenching cross sections of the 6s6p $^3P_0$ metastable state in atomic ytterbium with respect to helium and neon, and found them to be small enough to permit an Yb parity nonconservation experiment to be performed in a vapor cell. In addition, we have measured the pressure broadening and shift of the 649 nm 6s6p $^3P_0 \rightarrow$ 6s7s $^3S_1$ transition and the 556 nm 6s^2 $^1S_0 \rightarrow$ 6s6p $^3P_1$ transition. Future work will involve the specific design of an Yb vapor cell PNC experiment and construction of a new vapor cell with electric field plates. This new apparatus will allow us to further investigate the feasibility of an Yb PNC experiment in a vapor cell. In order to measure the quenching cross sections of the 6s6p $^3P_0$ metastable state, as opposed to finding upper limits, a better vacuum system and improved cell heating system will be employed. This will further eliminate gaseous impurities and allow better control of Yb density, reducing the systematic uncertainties associated with our imprecise knowledge of these parameters.

REFERENCES

Chapter One

[1] T.D. Lee and C.N. Yang, *Phys. Rev.* **104**, 254 (1956).

[2] C.S. Wu et. al. *Phys. Rev.* **104**, 1413 (1957).

[3] Ya. B. Zel'dovich, *Sov. Phys. JETP* **9**, 682 (1959).

[4] S.L. Glashow, *Nucl. Phys*., **22**, 579 (1961); S. Weinberg, *Phys. Rev. Lett.*, **19**, 1264 (1967); A. Salam, *Proceedings of the VIII Nobel Symposium*, N. Svartholm, ed., 367 (1968).

[5] F.J. Hasert, S. Kabe, W. Krenz, et. al., *Phys. Lett.*, **46B**, 121 (1973); A. Benvenuti, D.C. Cheng, D. Cline, et. al. *Phys. Rev. Lett.*, **32**, 800 (1974).

[6] M.-A. Bouchiat and C. Bouchiat, *Phys. Lett*. **48B**, 111 (1974); *J. Phys.* (Paris) **35**, 899 (1974); *J. Phys.* (Paris) **36**, 483 (1975).

[7] L.M. Barkov and M. Zolotorev, *JETP Lett.* **27**, 357 (1978); *JETP Lett.* **28**, 503 (1978); *Phys. Lett.* **B85**, 308 (1979).

[8] C.Y. Prescott, W.B. Atwood, R.L.A. Cottrell, et. al., *Phys. Lett.*, **77B**, 347 (1978).

[9] G. Arnison et. al., *Phys. Lett.* **126B**, 398 (1983).

[10] For thorough reviews of the subject, see:
D. Budker, in *WEIN-98 Conference Proceedings*, June 15-19, (1998);
M.-A. Bouchiat and C. Bouchiat, *Rep. Prog. Phys.* **60**, 1351 (1997);
D.N. Stacey, in *Atomic Physics 13*, H. Walther, T.W. Hansch and B. Neizert eds. (New York: AIP) 46 (1993);
E.D. Commins, *Physica Scripta* **T46**, 92 (1993);
P.E.G. Baird, in *Physics with Multiply Charged Ions*, ed. D. Liesen, NATO ASI, Series B:Physics **348** (New York: Plenum) 87 (1995);

[11] C.S. Wood, S.C. Bennett, D. Cho, B.P. Masterson, J.L. Roberts, C.E. Tanner, and C.E. Wieman, *Science* **275**, 1759 (1997).

[12] V.A. Dzuba, V.V. Flambaum, O.P. Sushkov, *Phys. Lett. A* **141**, 147 (1989); S.A. Blundell, J. Sapistein, W.R. Johnson, *Phys. Rev. D* **45**, 1602 (1992).

[13] V.A. Dzuba, V.V. Flambaum, O.P. Sushkov, *Phys. Rev. A* **56**, R4357 (1997); M.J. Ramsey-Musolf, in *Future Directions in Parity Violation*, 5th Annual JLAB (CEBAF)/INT Workshop, June 22-24, R. Carlini and M.J. Ramsey-Musolf eds. (1997); Review of Particle Physics. Particle Data Group (1996); W.J. Marciano and J.L. Rosner, *Phys. Rev. Lett.* **65**, 2963 (1990).

[14] S.C. Bennett and C.E. Wieman, *Phys. Rev. Lett.* **82**, 2484 (1999).

[15] W.C. Haxton, *Science* **275**, 1753 (1997).

[16] D. DeMille, *Phys. Rev. Lett.* **74**, 4165 (1995).

[17] C.J. Bowers, Ph.D. thesis, University of California at Berkeley (1998).

[18] J.E. Stalnaker, Undergraduate Thesis, University of California at Berkeley (1998).

[19] All energy levels in Yb are taken from W.C. Martin, R. Zalubas, and L. Hagan, *Atomic Energy Levels – The Rare Earth Elements* (NBS, Washington D.C., 1978), and references therein.

[20] V.A. Dzuba, V.V. Flambaum, and I.B. Khriplovich, *Z. Phys. D* **1**, 243 (1986).

[21] S.G. Porsev, Yu.G. Rakhlina, and M.G. Kozlov, *Pis'ma Zh. Eskp. Teor. Fiz.* **61**, 449 (1995); *JETP Lett.* **61** 459 (1995).

[22] B.P. Das, *Phys. Rev. A* **56**, 1635 (1997).

[23] E.N. Fortson, Y. Pang, and L. Wilets. *Phys. Rev. Lett.* **65**, 2857 (1990).

[24] Ya. B. Zel'dovich. *Sov. Phys. JETP* **6**, 1184 (1958).

[25] V.V. Flambaum and I.B. Khriplovich, *Sov. Phys. JETP* **52**, 835 (1980); V.V. Flambaum, I.B. Khriplovich and O.P. Sushkov, *Phys. Lett. B* **146**, 367 (1984).

[26] W.C. Haxton, E.M. Henley, M. J. Musolf, *Phys. Rev. Lett.* **63**, 1602 (1992); V.V. Flambaum, I.B. Khriplovich, O.P. Sushkov, *Phys. Lett. B* **146**, 367 (1984).

[27] M. Baumann, M. Braun, A. Gaiser, and H. Liening, *J. Phys. B.* **18**, L601 (1985).

[28] W. Lange, J. Luther, and A. Steudel, *Proc. 2nd EGAS Conf.* (1970) unpublished.

[29] C.H. Corliss and W.R. Bozman, *NBS Monograph* No. 53 (Washington, DC: US Govt. Printing Office) p.532 (1962).

[30] C.J. Bowers et.al. *Phys. Rev. A* **53**, 3103 (1996).

[31] F.H.K. Rambow and L.D. Schearer, *Phys. Rev. A* **14**, 738 (1976).

[32] J.-C. Keller and J.-L. Le Gouet, *Phys. Rev. Lett.* **52**, 2034 (1984); J.-C. Keller and J.-L. Le Gouet, *Phys. Rev. A* **32**, 1624 (1985).

[33] A.P. Ghosh, C.D. Nabors, M.A. Attili and J.E. Thomas, *Phys. Rev. Lett.* **54**, 1794 (1985).

[34] A.G. Yodh, J. Golub, and T.W. Mossberg, *Phys. Rev. A* **32**, 844 (1985).

[35] R.M. Lowe and P. Hannaford, *J. Phys. B* **22**, 407 (1989).

Chapter Two

[1] R.K. Marcus ed. *Glow Discharge Spectroscopies* (Plenum Press, New York, 1993).

[2] Starna Cells Inc., Atascadero CA, 93423.

[3] P. Camus ed. *International Colloquium on Optogalvanic Spectroscopy and its Applications*

(Les Editions de Physique, Cedex, 1983).

[4] J.E. Lawler, *Phy. Rev. A* **22**, 1025 (1980).

[5] Programmed in *LabVIEW*® by A.-T. Nguyen.

[6] M. Jacka, J. Kelly, B. Lohman, and S. Buckman, *J. Phy. B.* **28,** L361 (1995).

[7] R.W. Berends and L. Maleki, *J. Opt. Soc. Am B* **9**, 332 (1992).

[8] H. Schuler, J. Roig, and H. Korsching, *Z. Phys* **111**, 165 (1938).

[9] J.S. Ross and K. Murakawa, *J. Phys. Soc. Jpn.* **19**, 249 (1964).

[10] W.F. Meggers and J.L. Tech, *J. of Res. of NBS* **83**, 13 (1978).

[11] W. Whaling, M.T. Carle, and M.L. Pitt, *J. Quant. Spectrosc. Radiat. Transfer* **50** 7 (1993).

Chapter Three

[1] I.S. Grigoriev and E.Z. Meilikhov eds. *Handbook of Physical Quantities* (CRC Press, Boca Raton, 1997).

[2] Semco Laser Technology, Baldwin Park CA, 91706.

[3] M. Baumann, M. Braun, A. Gaiser, and H. Liening, *J. Phys. B.* **18**, L601 (1985).

[4] W. Lange, J. Luther, and A. Steudel, *Proc. 2nd EGAS Conf.* (1970) unpublished.

[5] C.H. Corliss and W.R. Bozman, *NBS Monograph* No. 53 (Washington, DC: US Govt. Printing Office) 532 (1962).

[6] J. Golub, Y.S. Bai, and T.W. Mossberg, *Phys. Rev. A* **37**, 119 (1988).

[7] E.L. Lewis, *Physics Reports* **58**, 1 (1980).

[8] I.B. Khriplovich, *Parity Nonconservation in Atomic Phenomena* (Gordon and Breach, Philadelphia, 1991).

[9] R.W. Berends and L. Maleki, *J. Opt. Soc. Am B* **9**, 332 (1992).

[10] H. Schuler, J. Roig, and H. Korsching, *Z. Phys* **111**, 165 (1938).

[11] J.S. Ross and K. Murakawa, *J. Phys. Soc. Jpn.* **19**, 249 (1964).

[12] D.L. Clark, M.E. Cage, D.A. Lewis, and G.W. Greenless, *Phys. Rev. A* **20**, 239 (1979).

[13] W.A. Wijngaarden and J. Li, *J. Opt. Soc. Am. B* **11**, 2163 (1994).

[14] J.H Broadhurst, M.E. Cage, D.L. Clark, G.W. Greenless, et.al. *J. Phys. B* **7**, L513 (1974).

Chapter Four

[1] C.J. Bowers et.al., *Phys. Rev. A* **59** (5), (1999); C.J. Bowers, Ph.D. thesis, University of California at Berkeley (1998). Available in electronic form at http://phylabs.berkeley.edu/bowers.

Chapter Five

[1] C.S. Wood, S.C. Bennett, D. Cho, B.P. Masterson, J.L. Roberts, C.E. Tanner, and C.E. Wieman, *Science* **275**, 1759 (1997).

[2] P.S. Drell and E.D. Commins, *Phys. Rev. A* **32**, 2196 (1985).

[3] C.J. Bowers et.al., *Phys. Rev. A* **59** (5), (1999); C.J. Bowers, Ph.D. thesis, University of California at Berkeley (1998). Available in electronic form at http://phylabs.berkeley.edu/bowers.

[4] S.C. Haydon ed., *An Introduction to Discharge and Plasma Physics* (University of New England, Armidale, 1964).

[5] D. DeMille, *Phys. Rev. Lett.* **74**, 4165 (1995).

[6] J.E. Stalnaker, Undergraduate Thesis, University of California at Berkeley (1998). Available in electronic form at http://phylabs.berkeley.edu/budker.